Morphological analysis of human cortical bone using high-resolution X-ray microtomography

Jalmari Pirhonen

Master's thesis
University of Jyväskylä,
Department of Physics
November 30, 2011

Abstract

Structural and elastic properties of bone are related to microstructural parameters such as porosity and anisotropy. Microtomography (µCT) enables assessment of bone microstructural geometry, typically down to a voxel size of 5 microns. The purpose of this thesis was to evaluate whether using a higher (sub-micrometer) voxel resolution in X-ray µCT enables detection of new, finer, details in human cortical bone. The second objective was to measure several morphological parameters that determine the microstructure, and to compare two different microtomographs. To this end, twenty four human cadaveric femur samples were imaged by Xradia XCT-400 at a voxel size of 0.56 - 0.59 µm and spatial resolution of 1.5 µm. For comparison, samples were measured by Skyscan 1172 at a voxel size of 2.78 µm. Scanner and image reconstruction parameters were individually tuned for each sample, so as to enhance the signal to noise ratio and to increase the amount of small detail. The systematical error due to the chosen procedure was satisfyingly low. Haversian canals (50.8 $\pm$ 25.4 µm) and ostecyte lacunae (3.74 $\pm$ 0.30 µm) were easily distinguishable from the scans by XCT-400, whereas SkyScan only extracted the Haversian canals. Morphological data from these two microtomographs had consistent distributions at the scale of the Haversian canals. Some correlations were observed between the morphological parameters, e.g. the cortical porosity correlated with pore diameter and number of pores. In conclusion, the Xradia µCT thus enables new level of bone morphological analysis which can enhance the understanding of relations between the properties of hierarchical microstructure and macroscopic features of the bone. Understanding of bone fragility can thereby be enhanced. In particular, such understanding plays important role in developing new methods of non-invasive bone assessment, based on quantitative ultrasound.

Preface

I would like to thank my supervisor Dr. Petro Moilanen for introducing me to this interesting topic. I am very grateful for the guidance and support throughout this work. My special thanks go to Prof. Jussi Timonen, Dr. Hanna Isaksson and the whole tomography group for invaluable support.

I would like to acknowledge my friends and colleagues in and out of the Physics Department. Many questions were answered at Holvi.

Finally, I would like to thank my mom and dad for the support, my brother for the neverending interest in my progress and Karoliina, who has always been there for me.

Tiivistelmä suomeksi

Osteoporoottiset murtumat vanhenevalla väestöllä aiheuttavat kansanterveydellisen ongelman niin Suomessa kuin muuallakin maailmalla. Yleisimpänä diagnosointimenetelmänä käytetään edelleen luun mineraalitiheyden määrittämistä DXA-laitteistolla. Nykyisen tekniikan avulla voimme havaita luuston ongelmat yleisimmin vasta murtumariskin kasvaessa, vaikka luustossa tapahtuvat rakenteellisten sekä elastisten ominaisuuksien muutokset viestivät mahdollisesta sairaudesta jo paljon aiemmin. Näiden ominaisuuksien mittaamista tutkitaan aktiivisesti ja tulevaisuudessa osteoporoosia ehkäisevä lääkitys on luultavasti mahdollista määrätä jo ennen varsinaisen taudin voimakasta etenemistä.

Luuston mikrorakenne on vahvasti sidoksissa luun elastisiin kertoimiin. Mikrorakennetta voidaan kuvata erilaisilla parametreilla, joista esimerkiksi huokoisuus ja anisotrooppisuus ovat keskeisiä. Tässä työssä mitataan 24 ihmisen reisiluusta kerättyä sylinterimäistä kuoriluunäytettä käyttäen Xradia XCT-400 mikrotomografialaitteistoa. Kuvien pikselikoko on $0{,}56 - 0{,}59\,\mu\text{m}$ ja erottelukyky $1{,}5\,\mu\text{m}$. Laitteiston sekä analyysiohjelmien säätäminen näytekohtaisesti vähensi selvästi kuvien kohinasuhdetta sekä paransi yksityiskohtien erottelua. Mineraalitiheyttä ei mittauksissa määritetty, sillä välttämättömät tiheysfantomit eivät mahtuneet näytteiden kanssa samanaikaisesti skannattavalle alueelle. Saaduista kuvista erottuivat selkeästi luun pitkittäissuunnassa kulkevat Haversin kanavat sekä tasaisesti jakautuneet pienet lacuna-ontelot.

Tomografialaitteistolla kuvatuista luunäytteistä määritettiin rakenteellisia ominaisuuksia kolmella eri tasolla: yksi sisälsi ainoastaan Haversin kanavien vaikutuksen, toinen ainoastaan lacunat ja viimeinen oli yhdistetty kahdesta mainitusta. Tilastollisen analyysin avulla ominaisuuksien välisiä yhteyksiä tutkittiin määrittämällä parametrien väliset korrelaatiokertoimet. Huokoisuuteen havaittiin vaikuttavan erityisesti huokoisten lukumäärä sekä halkaisija. Anisotrooppisuudella ei havaittu olevan merkittävää yhteneväisyyttä huokoisuuden kanssa ja rakenne-indeksi vaikutti huomattavasti ainoastaan yhdistelmätasolla. Suoritettuja mittauksia verrattiin yhteistyönä Itä-Suomen yliopistossa Kuopiossa eri laitteistolla tehtyihin mittauksiin. Yhteneväisyyksiä löytyi Haversin kanavien mittaluokassa.

Saavutettu hienorakenteen tarkkuus oli parempi kuin useimmissa tutkimuksissa esitetty. Mikrorakenteen tarkempi ymmärtäminen auttaa määrittämään makroskooppisia ominaisuuksia ja tarkentamaan mallia, jolla kuvataan luun kestävyyttä.

Contents

Abbreviations

µCT	Micro-computed tomography
3D	three-dimensional
BMC	Bone mineral content
BMD	Bone mineral density
BMU	Basic multicellular unit
BSE	Backscattered electrons
BUA	Broadband ultrasound attenuation
BV	Bone volume
Ca	Haversian canals
CCD	Charge-coupled device
CT	Computed tomography
CV	Coefficient of variation
DA	Degree of anisotropy
Dm	diameter
DPA	Dual photon absorbtiometry
DXA	Dual-energy X-ray absorptiometry
DXR	Digital X-ray radiogrammetry
ESD	Entrance surface dose
FBP	Filtered back projection
FOV	Field of view
HAP	Hydroxyapatite
JYU	University of Jyväskylä
Lc	Lacunae
MRI	Magnetic resonance imaging
N	Number
PBS	Phosphate buffered saline
qBEI	Quantitative backscattered electron imaging
QCT	Quantitative computed tomography
QUS	Quantitative ultrasound
RGB	Red, green, blue
ROI	Region of interest
S	Surface
SAM	Scanning acoustic microscopy
SD	Standard deviation
SEM	Scanning electron microscope
SMI	Structure model index
Sp	Separation
SS	Skyscan
SXA	Single X-ray absorptiometry
TLD	Thermoluminescent dosimeter
Co	Combined
TV	Tissue volume
V	Volume
WHO	World Health Organization
Xr	Xradia

1 Introduction

Osteoporotic fractures are a widespread and growing clinical problem globally and especially in modern welfare countries. Growing lifespan and changing lifestyle are major factors in the increasing number of osteoporotic fracture cases. As a disease osteoporosis is about alterations in geometrical (cortical thickness and cross-section area) and material (stiffness, mineral density and porosity) properties of bone [1]. These happen due to the imbalanced bone remodeling for which one of the most dramatic reasons especially for women is the drop of estrogen level during the menopause. The bone mass increases through childhood, and after the teenage years, where the peak bone mass is obtained, begins a natural state of osteoporotic bone resorption [2]. The degree of resorption is individual, but factors such as passive lifestyle and lack of sports, monotonous diet and shortage of calcium and vitamin D hastens the procedure.

Dual-energy X-ray absorptiometry (DXA) has the status of clinical standard for diagnosing osteoporosis [3]. In addition, the majority of all the clinical techniques are based on measuring the bone mineral content which is known to have a major effect on bone fracture risk. In osteoporosis not only the mineral content changes, but so does also the bone micro-architecture, characterized e.g. by porosity and bone volume fraction.

Microscopy enables observation of features smaller than those visible to the naked eye. On the other hand, with X-rays we can observe features inside structures. Computed tomography (CT) has made it possible to use X-rays to create three-dimensional (3D) visualizations, non invasively, of organs inside the human body. It enables digital assessment of bone micro-architecture. With high enough magnification it should be possible to detect even the smallest structural features. With this approach, one can quantify structural details of bone (e.g. volume and orientation of pores) at different hierarchical length scales. High resolution imaging also allows comparison between bones' structural properties and their mechanical features acquired by other methods. While medical and dentistry application remain the most common users of X-rays, they are also widely used in other applications such as airport security and industrial inspection.

This study was done in collaboration with the University of Eastern Finland (Kuopio), where a collection of human bone samples were assessed by X-ray microtomography at pixel size of 2.78 microns. The purpose of the present study was to evaluate, whether imaging at a higher resolution with pixel size of 0.6 microns is feasible for assessing finer structural details of the bone. To this end, the study was carried out in the X-ray tomography laboratory of the University of Jyväskylä.

A specific objective of the present thesis was to study, how a collection of cortical

bone samples from the human femur can be prepared and imaged with high resolution microtomography. A series of morphological parameters was determined from the imaged bone volumes by computerized analysis.

2 Bone and osteoporosis

2.1 Bone

Bone is a specialized connective tissue which forms, together with cartiledge, *the skeletal system*. At the organ level, the main functions of bones are to protect the vital organs and bone marrow, to provide a solid mechanical frame for muscles, so as to enable locomotion, and to be a metabolic reserve for nutrients such as calcium and continuous supply of new blood cells [4, 5].

Bone tissue is a composition of different materials such as minerals, water, cells and macromolecules such as lipids and sugars [6]. Material components of the bone can be classified into two main categories: organic and inorganic [4, 2]. The organic part includes type I collagens and some amorphous substance i.e. glycoproteins and proteoglycans. The inorganic part is constructed of different minerals, of which hydroxyapatite (HAP) $Ca_{10}(PO_4)_6(OH)_2$ is the main component with 68 % of the total mass of the bone. Together the cellular levels of organic and inorganic parts form the so-called bone matrix, which has all the features that make bone a special structure: flexibility, toughness, rigidity and compressive strength.

Bone has a hierarchical structure [7] (Fig. 1). Mineralized collagen forms long fibrils, which pack as fibers. These fibers form a *lamellar* structure, in which they are oriented randomly in layers [4]. This allows the highest density of collagen per unit volume of tissue. Lamellae can be either parallel or concentric, depending if they are deposited along a flat surface or surface surrounding a channel such as a blood vessel. In *woven bone* the fiber orientation is less organized. Woven bone occurs mainly at the early stages of bone growth and fracture repair [8].

Concentric lamellae (osteons or Haversian systems) surround an empty channel reserved for blood vessels [9]. These are known as *Haversian canals* and are connected to each other via oblique channels called *Volkmann's channels* [10]. Small *lacunae* are empty pores of former *osteocytes*, and *canaliculi* connects lacunae to one another. Osteocytes are former bone-forming cells (*osteoblasts*), which became trapped in the bone matrix and became calcified [4]. In Fig. 2 the structure of a bone and some typical sizes are presented.

At the tissue level, bone is constructed of two different forms: *cortical* (compact) and *trabecular* (cancellous) bone [12]. Compact bone forms the majority (about

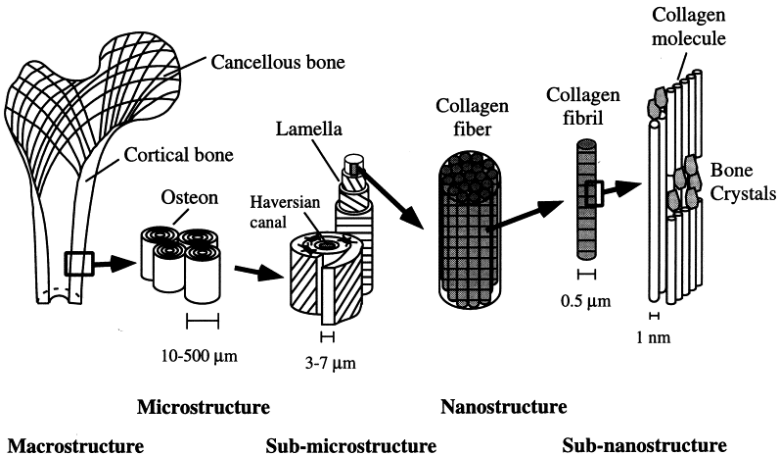

Figure 1. The hierarchy of bone structure: macrostructure: cortical and trabecular bone; microstructure: osteons with Haversian systems; sub-microstructure: lamellae; nanostructure: collagen fibers assemblies of collagen fibrils; sub-nanostructure: bone mineral crystals, collagen molecules, and non-collagenous proteins [7].

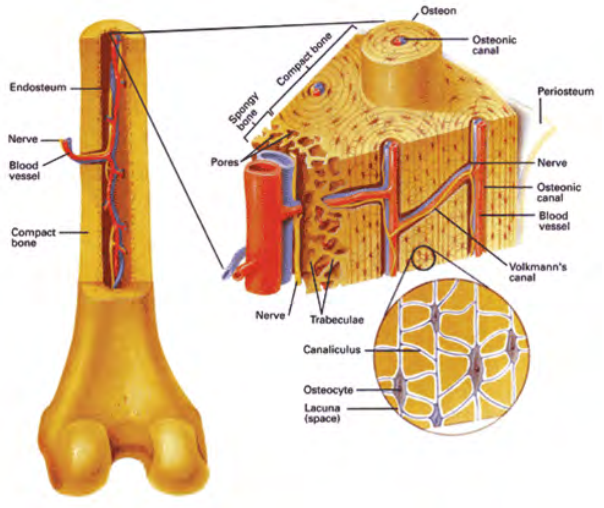

Osteons	500 µm diameter
Trabeculae	200 µm thick
Haversian canals	100 µm diameter
Lacunae	10 µm diameter
Lamellae	5 µm thick
Cement lines	1-5 µm thick
Canaliculi	1 µm diameter
Collagen fibers	3 µm long, 15 nm diameter
Mineral crystals	300 · 30 nm plates

Figure 2. The structure of a bone and some values of size for different components [11]. Also some typical sizes of bone structures are shown.

85 %) of human skeleton. Because of its high density ($\rho = 1.7 - 2.0\,\mathrm{g/cm^3}$) and stiffness that comes from the material and configuration, it can be found on periosteal parts of almost any bone. Long bones like tibia and radius are mostly cortical bone [12]. Trabecular bone can be found at the ends of long bones and in the cores of flat bones like scapula and vertebrae. As a softer material, trabecular bone has the capability of compression without permanent damage when decent stress is applied. Trabecular bone is always coated with cortical bone and together they form a rigid but flexible body which can absorb impacts without breaking. Trabecular bone is composed of an interconnected network of bone plates, struts and rods surrounded by bone marrow [13], which is where *hematopoiesis*, the production of blood cells, occurs [2]. The primary structural difference between cortical and trabecular bones is quantitative: the calcification percentage is $80 - 90\,\%$ for cortical and only $15 - 25\,\%$ for trabecular bone [4].

2.2 Bone remodeling: growth and aging

Bone tissue overcomes continuous process of creation and resorption (i.e. bone turnover) of the bone matrix. Two types of bone cells, *osteoblasts* and *osteoclasts*, are mainly responsible for this bone remodeling. Osteoblasts take care of the production of the bone matrix constituents by forming HAP and other minerals into lamellar structure [4]. When osteoblasts become surrounded by the bone, they mineralize and transform into osteocytes. Although they are quite inert cells they still have some functions: they destroy bone material through osteocytic osteolysis, they control the activity of osteoblasts and osteocytes within basic multicellular unit (BMU) and they are connected to each other via cytoplasmic extensions through small canaliculi to exchange nutrients and waste [4, 6]. Osteoclasts are large bone-lining cells responsible for bone resorption [14].

Bone growth can be described with two different mechanisms, *endochondral ossification* and *intramembranous ossification* [4, 15]. Endochondral ossification is responsible for longitudinal growth where new cartialedge is constantly formed in a region called physis. This region moves and its diameter stays constant as physis mineralizes at the same rate as new bone is formed. This happens mainly for long bones. Intramembranous ossification means growth in diameter which is needed in flat bones and it is also the main factor in bone modeling and remodeling. By removing and rebuilding bone can adapt to different loading conditions during the lifetime.

For a healthy individual, bones grow in size and mass through puberty, where the peak in these features is obtained [16]. Thereafter a gradual loss of bone takes place. Bone growth diminishes and bone remodeling starts to adapt bones to different conditions. The ratio between bone formation and resorption is dependent on

mechanical stimulation (environment) of the bone as well as hormonal effects, nutritional changes and gene inheritance [17]. This leads us to the difference in bone loss between males and females. Women lose about $35-40\,\%$ of the cortical bone and $55-60\,\%$ of the trabecular bone when the corresponding values for men are about one third smaller [16].

During aging the red marrow, which contains hematopoietic tissue, is gradually converted into yellow bone marrow, which is mainly made of fat cells [18].

2.3 Osteoporosis

Osteoporosis is defined as a metabolic bone disease characterized by low bone mass and micro-architectural deterioration of bone tissue leading to enhanced bone fragility and a consequent increase in the fracture risk [19]. Osteopenia is a preliminary stage of osteoporosis for which the osteoporotic changes in bone properties can be regarded detectable. Osteomalacia is, another common metabolic bone disease, characterized by relative deficiency of mineral contents in relation to collagen while in osteoporosis this ratio is unaffected.

Osteoporosis results in increasing porosity of the trabecular matrix or increasing porosity and decreasing thickness of the cortical wall [16, 20]. As a result, ability of bone to resist fracturing in tensional, compressional, bending or torsional loading decreases. This leads to increased risk of fractures, especially in bone sites which are under big stress, the femoral head or lumbar spine, for example. An example of the difference between healthy and osteoporotic bone has been illustrated in Fig. 3.

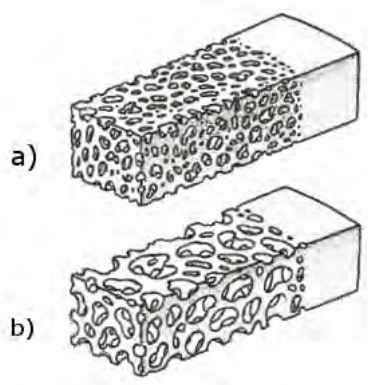

Figure 3. A sketch of a) normal healthy bone and b) osteoporotic bone [5]. In osteoporotic bone the cortical wall thickness decreases and the porosity as ratio between pore volume and tissue volume increases.

Three subtypes of osteoporosis can be distinguished depending on the causing factors of bone deterioration: postmenopausal, senile and secondary osteoporosis [21]. Postmenopausal osteoporosis affects women between the ages of 50 and 65 years. Estrogen has a major role in regulating the bone remodeling cells. During the menopause estrogen level declines, which leads to decreased activity of osteoblasts while osteoclasts remain active. Senile osteoporosis affects mostly after the age of 70 and is as common for both men and women [8]. It can be observed as loss of both cortical and trabecular bone mass. Secondary osteoporosis is the same disease without age references and is a result of different factors listed below [22, 3, 23]. These can be applied for both osteoporosis and fragility fractures.

- Female gender
- Age
- Hypogonadism
- White race
- Low body mass index
- Familial prevalence
- Previous fragility fracture
- Smoking
- Low physical activity
- Menopausal age
- Obesity
- Low dietary calcium intake
- Vitamin D deficiency

2.4 Clinical bone assessment

Increased fracture risk is typically characterized by the reduced areal bone mineral density (BMD) and areal bone mineral content (BMC), assessed by DXA [23]. BMD refers to the amount of mineral per square centimeter of the bone. It can be measured from any skeletal site, which gives a valuable estimation of the universal state of the skeleton, or measured from an exact site like hip, which gives a specific evaluation of the bone status at this skeletal site, where fractures predominantly occur.

Diagnosis of osteoporosis is typically based on the so-called T-score. This parameter is determined against normative data for young healthy adults and it enables, by definition, comparison between different measuring techniques [3]. T-score is expressed by [22]:

$$T = \frac{X - Xy}{young\ adult\ standard\ deviation}, \tag{1}$$

where X is the patient's BMD, Xy is the average peak BMD for the healthy young reference population of the same gender and the denominator represents the standard deviation (SD) of the same reference population. Criteria made by

Table 1. WHO criteria for the diagnosis of osteoporosis based on BMD [3].

Category	Criteria	T-score
Normal	A value of BMD within 1 standard deviation below the young adult mean, but less than 2 standard deviations below this value.	≥ -1
Osteopenia, low bone mass	A value of BMD more than 1 SD below the young adult mean, but less than 2 SD below this value.	< -1 and > -2.5
Osteoporosis	A value of BMD 2.5 SD or more below the young adult mean.	≤ -2.5
Severe osteoporosis	A value of BMD 2.5 SD or more below the young adult mean in the presence of one or more fragility fractures.	

World Health Organization (WHO) define normality and the state of osteoporosis in T-score units (Table 1).

Another parameter, Z-score, is used to put the patient's BMD in perspective by comparing to the normative data for the same age group. This is useful for the elderly patients, who would be osteoporotic by the T-score, but average for their own age [22]. The Z-score is expressed by

$$Z = \frac{X - Xa}{population\ standard\ deviation}, \tag{2}$$

where Xa is the mean BMD for persons of same age and gender.

In addition to organic and inorganic material, bone consists of a significant amount of water, which contributes to the X-ray absorption [10]. When determining the BMD, depending on the method used, there are some assumptions used that may lead to inaccuracies. In the worst case the soft tissue composition, bone structure and bone shape can result in an up to 35 % error in BMD measurements [24]. Also, inaccurate patient positioning, scan analysis or mistakes in interpretation adds the inaccuracy.

2.5 Modalities of clinical densiometry

Historically, BMD has been measured by using gamma radiation, but fortunately other options are nowadays available including DXA as the clinical standard. With

DXA, measurements can be obtained from any site in the body, although the standard sites of diagnosis are the proximal femur (hip) and lumbar vertebra (spine) [10]. The WHO standard T-score is highly based on this technique, although it can be applied to any other method as well [3].

DXA was developed from *dual photon absorptiometry* (DPA) [25]. Though they both have the same physical principles, the production of photons differs between these methods. In DPA a radionuclei source is used while in DXA an X-ray tube produces the photons. The basic principle in measuring BMD with DXA is to measure the photon absorption using two different energies, typically 40 and 70 keV. Both the BMD and the overlying soft tissue are evaluated at the same time. *Single X-ray absorptiometry* (SXA) is a predecessor for the DXA with only one X-ray beam in use during measurements [3].

Digital X-ray radiogrammetry (DXR) is a fairly easy and cheap way of measuring bone mineral content [26]. By measuring the outside and inside diameters of the cortex for the three middle metacarpal bones in hand, the cortical thickness, cortical area and percentage of the cortical area can be calculated. This method is good to be used especially for children, since the skeletal age can also be determined. In addition to calculation of cortical thickness, these measurements can be used to evaluate whether the bone loss is due to endosteal resortion or lack of periosteal surface apposition. Disadvantages are that DXR does not measure cancellous bone and so does not recognize bone loss within cortex.

Quantitative computed tomography (QCT) relies on X-ray absorption measurements on well-defined volumes instead of two-dimensional projections [26]. Usually the X-ray source and the detectors are rotating around the patient. A three-dimensional illustration can be reconstructed from the absorption projections at different angles [10]. A calibration phantom is required to be imaged simultaneously with the patient to ensure standardization and thus to correct the readings of the BMD analysis. Major advantages at QCT are the ability to assess cancellous bone density due to volumetric density and high resolution (image pixel size is about 300 µm [10]) [3]. Also, the geometry of an entire bone can be modeled. A disadvantage is that BMD has been shown to be dependent on the bone marrow composition, which differs from the chemical analyses made on the same object. The cost of the equipment is also expensive and the radiation dose to the patient is even bigger than in DXA measurements.

Magnetic resonance imaging (MRI) of bones is still at a development stage. Due to lower radiation dose it could be an option for high resolution imaging of trabecular bone [3]. Although it does not give any information about the density of the bone, it provides a view of the internal structure of cancellous bone with the positive background given by all types of bone marrow. Its downside is that measurements

are complex and highly expensive.

Research on *skeletal quantitative ultrasound* (QUS) has been active and the method has been suggested as an alternative option by a number of studies [27]. As the most important aspect we get information about geometrical as well as material properties (e.g. mineralization, porosity and Young's modulus) [28]. Ultrasonically these bone properties are typically characterized by a measured velocity of one or more wave modes. In addition, some QUS techniques may assess bone by parameters such as broadband ultrasound attenuation (BUA) and backscatter coefficient. Advantages of QUS compared to other methods are inexpensiveness, mobility and safety of measurements for the patient since there are no ionizing radiation sources used.

All of the mentioned techniques have their pros and cons. Since bone mass may be discordant at various skeletal sites in an individual patient, and because different techniques give different results even at the same site for a single patient, T-scores cannot be used interchangeably with different techniques or at different sites [22]. Some features of different methods to detect osteoporosis are given in Table 2.

2.6 Microstructure imaging

In clinical methods the contribution of bone quality and quantity is somewhat disregarded although they both play a major role in bone strength and fracture risk assessment. Nowadays there are several noninvasive and nondestructive methods which concentrate on different levels of microstructure in the hierarchical structure of bone. Besides the small geometric detail of canals and lacunae (Fig. 2), many features such as trabecular volume, trabecular spacing, cortical porosity and connectivity can be acquired. These are related to bone strength as much as the BMD.

Table 2. Comparison of different modalities for assessing bone [22, 8].

Factor	DXA	QCT	QUS
Cost	Intermediate	High	Low
Radiation dose	Low	High	None
Portability	Limited	No	Yes
Parts measured	Spine, hip, wrist	Spine, hip	Calcaneus, radius, tibia
Precision	Excellent	Good	Moderate
Monitoring of treatment response	Good	Good	Low

Techniques most commonly used for micro-architectural analysis of bone are micro-computed tomography, scanning acoustic microscopy and scanning electron microscopy.

Micro-computed tomography (micro-CT or µCT) is used for detailed imaging of bone structure beyond the capabilities of conventional (clinical) QCT. Pixel size (or voxel size in 3D) of the image can be down to sub 1 µm. At this scale it is possible to distinguish osteocytes inside the bone composition. Yet finer imaging at sub 0.1 µm scale can be done by nano-CT, so as to enable 3D assessment of e.g. the mineral distribution (i.e. the degree of mineralization [29]). At this point the related tomography devices are purely academic and can be used only for small dried samples separated completely from the soft tissue. Analysis of bone micro-architecture based on high resolution X-ray tomography is described in more detail in Chapters 3 and 4.

Scanning acoustic microscopy (SAM) is used to detect and map elastic properties of bone by measuring acoustic impedance over tissue surface [30, 31]. SAM works by directing focused high-frequency ultrasound (typically 50 MHz to 1 GHz or more) on the surface of the object, e.g. cross-section of the bone. The frequency determines the resolution of imaging . For example, in a commercial device using an ultrasonic transducer with a nominal frequency of 150 MHz, the spatial resolution is about 10 um [32].

Scanning electron microscope (SEM) uses a beam of electrons swiping over the surface of the sample. With SEM both structural and analytical information of bone can be obtained, such as information about bone resorption, surface structures and cell-matrix interactions [33]. Secondary electron diffraction is commonly used in all SEMs but they can also use backscattered electrons (BSE), characteristic X-rays, cathodoluminesence, specimen current and transmitted electrons. A crucial benefit of SEM is its magnification which can reach from 10 to even 500,000 at best. Optical microscopes use magnifications from 10 to about 2,000.

The degree of mineralization of trabeculae can be measured with a special BSE technique called *quantitative backscattered electron imaging* (qBEI). It is a high resolution quantification and visualization technique in which the backscattered electrons detect differences in atomic number and thus in the mineral content of the sample surface [34]. Mineralization dictates the material properties such as the Young's modulus and yield strength of bone. Often this method is being used alongside the characteristic X-rays, because they both are strongly related to the atomic number of the specimen.

Another measurement technique for the mechanical properties of bone is *nanoindentation*. A sample surface is studied with indentation using a tip of known shape

while monitoring the applied load and displacement [35]. A common tip shape is a three-sided pyramid, the 'Berkovich tip'. Usually SEM or SAM is needed to provide sufficient accuracy for the tip's location. With nanoindentation attributes such as Young's modulus, hardness and strain-rate dependence can be measured.

3 X-ray imaging

X-rays cover part of the electromagnetic spectrum withing a range of wavelengths from 0.01 to 10 nm, corresponding to energies of 150 to 10 keV, respectively [36]. X-rays are generated when light, or charged high-energy particles lose their speed rapidly when hitting particles of high atomic number, i.e. of large mass for instance. X-rays of high energy can penetrate non-metallic substances fairly easily, and this is why they are generally used in many fields of industry and in clinical studies. X-rayswere discovered in 1895 by a German scientist, William Röntgen.

3.1 Producing X-rays

A Common way of producing X-rays is the X-ray tube, a vacuum tube shown in Fig. 4. A glass casing contains a cathode and an anode [36]. An electron beam is emitted from the cathode towards the positively charged anode by applying a potential difference of 15 to 150 kV between them. The disk shaped anode is usually made of tungsten since the anode material has to have a high melting point (3410 °C for tungsten [37]), good thermal conductivity and low vapor pressure (10^{-7} bar at 2250 °C, lowest for all metals). The anode plate is usually spinned for a longer lifespan and to reduce erosion by increasing cooling time. Vacuum gives electrons a disturbance free trajectory to the anode and prevents the filament from burning.

The energy at which electrons are drawn from the cathode towards the anode is comparable to the voltage difference U between these. The amount of electrons can be expressed with the current (I) which flows through the X-ray tube. The radiation power P at which the device operates is determined by I and U.

When electrons hit the anode, their direction is changed and speed reduced. From the total energy generated, 99 % becomes heat and only 1 % is converted into electromagnetic radiation due to the *bremsstrahlung effect*, which we call X-rays or braking radiation [38]. This phenomenon is basically such that electrons unleash their kinetic energy as electromagnetic radiation. The energy spectrum of the bremsstrahlung radiation is continuous. Impacting electrons excite electron states of the anode atoms. Characteristic radiation is generated when atoms in the anode discharge these excited states. When this happens at the K shell of atoms (the

innermost electron shell of an atom, Fig. 5), the emerging characteristic lines are called K-lines. The incoming electron must have an energy greater than 70 keV to eject a K shell electron from the anode. Discharge of other shells happens as well, but we can take into account only the K lines as they typically have a higher intensity than the rest. These lines are unique for the anode material. Both bremsstrahlung and characteristic X-ray radiation can be seen in Fig. 6.

There is no characteristic radiation below an operating energy of 70 kV, but within the range 80 to 150 kV, characteristic radiation covers $10 - 30\,\%$ of the total intensity of the spectrum.

The spectrum radiation power (P) is given by the equation [36]

$$\frac{dP}{dE} = CZI\left(E_m - E\right), \tag{3}$$

for $0 < E \leq E_m$, while

$$\frac{dP}{dE} = 0, \tag{4}$$

for $E > E_m$.

Here E is the photon energy, E_m is the kinetic energy of the electrons ($E_m = eU$, e is the electron charge), Z is the atomic number of the anode material and C is a constant. Integration of Eqs. (3) and (4) gives

$$P = kZIU^2, \tag{5}$$

where $k = Ce^2/2$ is a constant.

3.2 X-ray scattering

X-rays passing through a human body, or some other object, can be categorized into three separate groups [38]. X-rays that do not interact with the tissue are called primary radiation. Secondary radiation consists of X-rays scattered by the tissue, by different mechanisms that alter trajectories of X-rays. Finally, X-rays can be absorbed completely in the tissue so that they do not reach the detector.

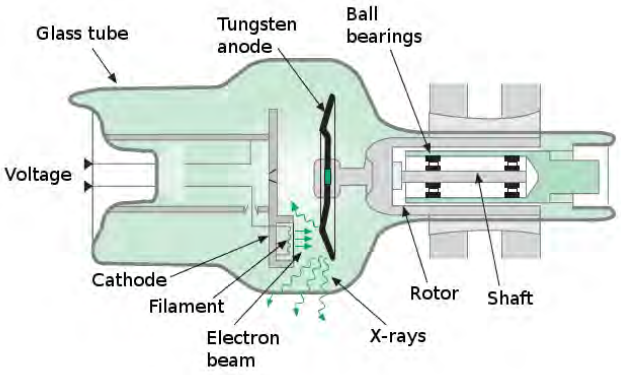

Figure 4. An X-ray tube and its basic components. Electrons emitted from the cathode hit the tungsten anode. Only a small amount of the energy generated is emitted as X-rays when the rest is emitted as heat [36].

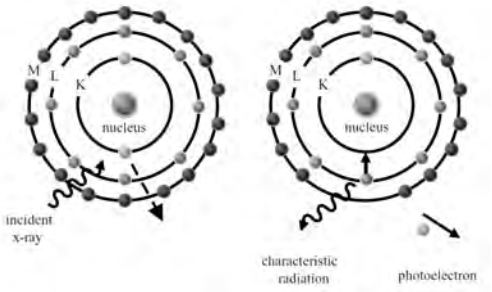

Figure 5. Formation of characteristic radiation via photoelectric interaction when an incident X-ray excites a K-shell electron [38].

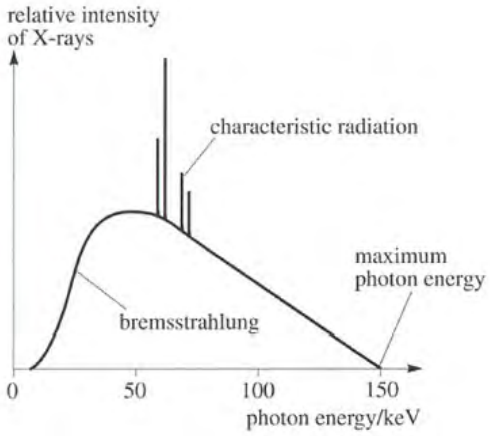

Figure 6. A typical energy spectrum of an X-ray tube with a tungsten anode. Notice the K-lines of tungsten, which appear as spikes in the otherwise continuous spectrum. The K lines do not move although the operating energy (i.e. voltage U) would be changed. In this case only the bremsstrahlung line would grow or diminish depending on the energy change (increase or decrease, respectively).

There are three main mechanisms in the formation of secondary radiation [38]. *Coherent scattering*, also called Rayleigh scattering, represents nonionizing interaction between X-rays and the tissue. The energy of an X-ray is converted into oscillations inside an atom, which are relaxed by emission of a secondary X-ray with the same wavelength but in a random direction.

Compton scattering refers to interaction between an incident X-ray and an electron on the outer shell (usually M shell) of an atom. A part of the X-ray energy is transferred onto this electron which is ejected. The energy of the scattered beam can be calculated by applying the laws of conservation of momentum and energy. For the conservation of momentum (p) we have [38]

$$p_{e,free} = p_{X,inc} - p_{X,scat}, \tag{6}$$

where the subscripts are: e for electron, X for the X-ray beam, inc for incident beam, $scat$ for scattered beam and $free$ for the free electron. For the energy we have

$$E_{X,inc} + E_{X,bound} = E_{X,scat} + E_{e,free}. \tag{7}$$

Combining Eqs (6) and (7), we can find the energy of the scattered beam in the form

$$E_{X,scat} = \frac{E_{X,inc}}{1 + \left(\frac{E_{X,inc}}{mc^2}\right)(1 - \cos\theta)}, \tag{8}$$

where m is the mass of the ejected electron and c is the speed of light.

Consider an X-ray deflected by angle θ. If θ is sufficiently small, the energy of the deflected beam is nearly the same as that of the incident beam. Nevertheless, the beam is off its original path, but is detected with approximately the same efficiency as the primary radiation.

The third category of secondary radiation is produced by the *photoelectric effect*: when an X-ray is absorbed by an atom in the tissue, a tightly bound electron is emitted from the K or L shell as a photoelectron [38]. A second electron from a higher energy level fills the created hole and emits a characteristic X-ray with an energy equal to the difference in the binding energy of the outer electron and the emitted photoelectron. This process is illustrated in Fig. 5. The probability of photoelectric attenuation of X-rays drops off rapidly as a function of the incident X-ray energy.

3.3 Attenuation and filtering

Attenuation of the X-ray spectrum is nearly similar to that of gamma rays. As an example, for monochromatic radiation we have an exponential attenuation derived from the Beer-Lambert law [39]:

$$I = I_0 e^{-\mu(E)d}, \tag{9}$$

where I and I_0 are the intensities of the transmitted and incident X-rays, respectively, μ is the linear attenuation coefficient (sum of the different interactions) and d is the thickness of the material. Thus the intensity of the X-rays is dependent on the density and thickness of the material it is passing through. In Fig. 7 one can observe linear attenuation coefficients for different X-ray interactions, and mass attenuation coefficients for different tissue types. In an X-ray image, bone is visible due to different interactions from those in muscle and fat which cannot be separated easily because of similar composition.

It is useful to reduce some parts of the energy spectrum of the radiation by filtering. Some filtering happens already at the X-ray tube, when radiation is guided out of the tube through a beryllium window. The lower end of the energy spectrum can be suppressed with additional filtering layers after the radiation source. The filtered part of the spectrum would be absorbed in the object and would not reach the detector anyway. After all, the useful information about the absorption inside the object is in the detected beam. Filters most commonly used are made of glass or metals like aluminium or copper. The filtering factor depends on the material and thickness of the filter. For commercial use filter kits, including a collection of filters, are available.

The efficiency of a filter can be expressed as a sum of mass attenuation coefficients, which can be derived from distance attenuation coefficient μ and density ρ of each medium by the following equation [36]

$$\frac{\mu(E)}{\rho} = \sum_i \left(\frac{\mu(E)}{\rho}\right)_i \cdot w_i, \tag{10}$$

where $\left(\frac{\mu(E)}{\rho}\right)_i$ is the mass attenuation coefficient for element i and w_i is its mass fraction in percents in the medium.

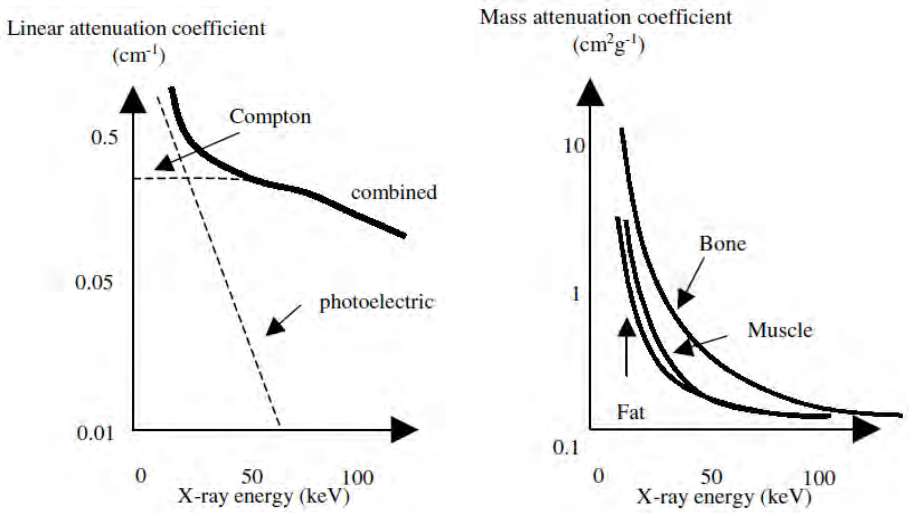

Figure 7. a) The linear attenuation coefficient shows how the operating energy affects the Compton scattering and the photoelectric effect. Coherent scattering is ignored due to its small effect. b) Mass attenuation coefficient showing the difference between body materials. For low energies the probability for photoelectric interactions is much higher in bone than in tissue because bone contains calcium, which has a relatively high atomic number. Muscle and fat contain high amounts of water and so have relatively consistent structure, and thus similar mass attenuation coefficients [38].

3.4 Detecting the X-rays

After interacting with tissue, X-rays must be detected. The main challenge of detection is extraction of the useful information, related to tissue properties, from e.g. noise. This procedure is typical in everyday X-ray imaging.

A collimator, or beam restrictor, is usually located between the source and the object [38]. The purpose of this is to adjust the radiation field to match the field of view (FOV). FOV is dependent on the detector and its surface area. The main function of the collimator is to decrease the beam flux and thus the radiation dose of the patient since beams outside the FOV have no value for the image.

Due to the effect of different X-ray interactions, some parts of the beam deflect inside the object, depart from their original paths and are distributed randomly over the detector. This phenomenon reduces the resolution of the image. An antiscatter grid can be placed between the object and detector so as to absorb the deflected part of the beam. This grid consists of strips of lead foil which are oriented in the

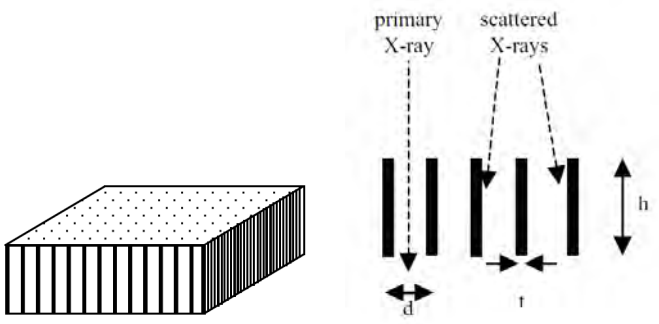

(a) (b)

Figure 8. a) A schematic presentation of an antiscatter grid to absorb scattered X-rays. b) Definition of h, t and d for the grid ratio and strip line density [38].

direction of primary radiation and supported by a low attenuating medium like aluminium or plastic for example. The properties of the grid are described in terms of grid ratio and strip line density such that [38]

$$grid\ ratio = \frac{h}{d} \tag{11}$$

$$strip\ line\ density = \frac{1}{d+t}, \tag{12}$$

where h, t and d are the length and thickness of the strips and distance between the centers of the strips, respectively (Fig. 8). Typical values for the grid ratio vary from 4:1 to 16:1 and for the grid line density from 25 to 60 per cm.

In the past, the most widely used detector, especially in clinical studies, was a photographic film or plate which recorded the passing X-rays. These accessories contain silver halides, similar to those in photographic films, so as to record visible light passed through the camera lens. Since the film or plate must be developed and replaced after each exposure, this approach has been replaced by a semi-digital method. In the new approach X-rays are recorded on a photostimulable, phosphor-based imaging plate containing fine-grain barium fluorohalide crystals doped with divalent europium (Eu^{2+}) [38], and the image data are transferred digitally onto a computer by laser reading the excited electrons. Such plates can be erased from all image data by visible light, and can thereby be reused numerous times.

Also fully digital detectors, with sensors based on a *charge-coupled device* (CCD), similar to those in digital cameras, have become popular. A CCD sensor is essentially a metal oxide semiconductor, usually constructed of p-doped silicon as the conducting material and silicon oxide as the insulator. When photons hit the photoactive epitaxial layer of silicon (an array of capacitors known as photosites or pixels [40]), each capacitor accumulates charge proportional to the light intensity. Information in the form of electric charge is transferred along the silicon surface in "clocked shift register" fashion by manipulating the voltages on the control electrodes sequentially [41]. The last capacitor of the array dumps its charge into a charge amplifier to convert the charge into voltage. This series of voltages is sampled, digitized and stored in the memory. Figure 9 illustrates a capacitor array that moves the charge towards its end. All the data that are stored for each exposure time is saved as one picture.

3.5 Spatial resolution

Spatial resolution defines how close are lines that can still be resolved in an image. Many things affect spatial resolution, including thickness of the intensifying screen [38] and properties of the system creating the image. The clarity of the image is characterized by its spatial resolution rather than the number of pixels in the image. Unlike the usual beliefs in the consumer market, the pixel resolution (usually counted as pixels per inch, *ppi*, or pixel amount in megapixels) is not the only factor affecting the image clarity. True spatial resolution can be determined by imaging different test patterns. One approach, still widely used, is the 1951 USAF resolution test chart conforming to the MIL-STD-150A standard, originally set by US Air Force. In this chart three vertical and three horizontal lines are positioned next to each other so that the space between the lines are the same as the width of a single line. Starting from the first set, the width of the lines starts to decrease. The largest bar that the device cannot discern sets the limit to the resolution (Fig. 10). These charts are commercially available in sizes specially defined for any imaging device. It is possible to carve the lines onto a metal surface at almost any scale, using a laser for instance.

Although an X-ray source is considered point-like, it has a finite size. This results in the phenomenon known as geometric unsharpness. It causes some blurring in the image, which is most apparent at the edges of different tissues. In this case the effect is called *penumbra* or half-shadow. The degree of image blurring is dependent on the effective focal spot size, f, the distance between the object and the X-ray source, S_0, and that between the source and detector, S_1. In Fig. 11 we illustrate

the formation of blurring. The size of the penumbra is given by [38]

$$P = \frac{f\,(S_1 - S_0)}{S_0}. \tag{13}$$

To increase image quality, S_0 should be as long and f as small as possible.

From distances S_0 and S_1 we also get the magnification factor, m, such that

$$m = \frac{S_1}{S_0}. \tag{14}$$

3.6 Radiation dose

X-rays feature energetic ionizing radiation which can cause damage to living tissue. The main risk of such radiation is development of cancer as a result of genetic mutations caused by chromosomal aberrations. The direct (deterministic) effect of high dose is cell death while lower doses affect stochastically the probability of damage occurrence.

The absorbed dose, D, is consistent with the energy (E) of the radiation absorbed per unit mass [36]. D is typically expressed in grays Gy ($1\,\mathrm{Gy} = 1\,{}^{\mathrm{J}}/_{\mathrm{Kg}}$) or rads ($1\,\mathrm{Gy} = 100\,\mathrm{rad}$). Typical doses in taking clinical radiographs are measured in mGy's. In clinical use it is convenient to express the radiation dose by an effective dose equivalent, H_E, which has the unit of sievert (Sv) and is usually measured in mSv's. H_E is given by

$$H_E = \sum_i w_i H_i, \tag{15}$$

where i is the organ considered, w_i is the related weight coefficient and H_i is the dose equivalent for that organ or tissue type. H_i is dependent on the absorbed dose, D, and a quality factor which is different for each type of radiation (X-rays, neutrons etc.). Some values of w_i for different tissue types are shown in Table 3.

The effective dose absorbed by an individual cannot be directly measured. Doses related to different types of clinical imaging are based on approximations. Some typical effective radiation doses are shown in Table 4.

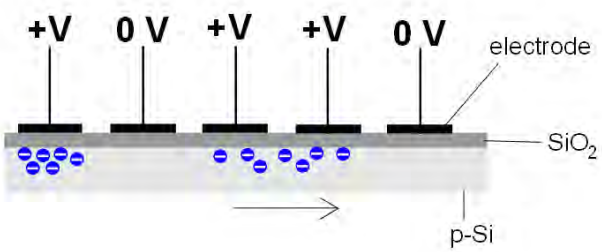

Figure 9. CCD moving electrons sequentially by applying potential difference to metal electrodes. An insulating layer of silicate oxide (SiO_2) separates the charge and the electrode. The last one is an 'output gate' where the charges are converted into voltage signals.

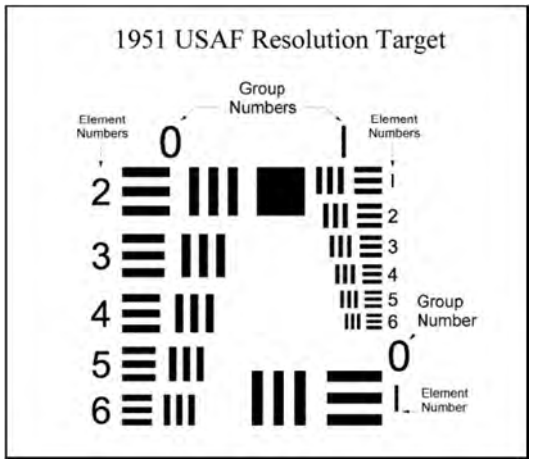

Figure 10. The USAF 1951 resolution chart for detecting optical resolution of an imaging device [42]. Group and element numbers are for identification of the resolution limit.

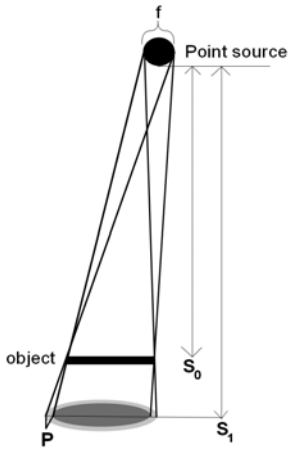

Figure 11. Half shadow or penumbra (P) is cast around an object (light grey area). If f is small and S_0 is big, especially compared to $(S_1 - S_0)$ the effect of penumbra becomes smaller.

Table 3. Effective dose weight factor values for different tissue types. These values are defined for the average population composed of even number of men and women and with a broad age spectrum [36].

Tissue or organ	weight factor w_i
Testicles	0.20
Bone marrow	0.12
Lungs	0.12
Large intestine	0.12
Stomach	0.12
Liver	0.05
Thyroid gland	0.05
Oesophagus	0.05
Breast	0.05
Bladder	0.05
Bone surface	0.01
Skin	0.01

Table 4. Average effective radiation doses for an individual, exposed to different types of clinical radiological assessments [36]. These values are highly approximated since the exact doses feature significant individual variation.

X-ray	Effective dose (mSv)
Limbs	< 0.001
Dental tomography	0.004
Chest	0.1
Skull	0.12
Mammography	0.2
Hip	1.3
CT	
Head	1.3
Chest	5.1
Angiographs	$1.0 - 25$

Patient's radiation dose is not a trivial thing to measure. Some studies have evaluated the radiation dose by using *thermoluminescent dosimeters* (TLD) inside layered phantoms, although such results cannot unambiguously be applied to real situations. The effective dose can be evaluated from the measured phantom dose, risk factor of each organ and *entrance surface dose* (ESD).

4 Micro-computed tomography

Micro-computed tomography has become a standard technique for visualization and quantification of the three dimensional (3D) structure of trabecular bone. To date, technical development and decreasing prices of the scientific devices have made it possible to explore structures at the sub 1 µm scale. Even though it is not really possible to detect mineral orientation (nano-CT is required), microstructure of the bone can be identified down to the length scale where osteocytes and canaliculi can be observed. Osteocytes provide valuable information about the state of

bone reformation and porosity, both of which are crucial factors characterizing osteoporosis and affect many other clinically measurable parameters such as ultrasound velocity.

X-ray microtomographs form images based upon X-rays transmitted and propagated through the sample. The less X-rays the sample absorbs, the brighter the image becomes. Absorption increases with increasing density, thickness and other material properties. Micro-CT produces absorption images, i.e. shadowgrams (Fig. 12a), of the scanned object. The quality of the image is dependent on several factors such as the object's dimensions, spatial resolution, magnification, number of imaging angles and exposure time. The set of shadowgrams is processed and reoriented in a phase called *reconstruction*, so as to provide a stack of cross-sectional 'slices' representative of the structure through the imaged sample (Fig. 12b). The most important reconstruction algorithm in tomography is the *filtered back projection* (FBP) algorithm. The idea is to convert the propagation of the X-ray beams into an inversion problem by using the Radon transform $\mathbf{R}$ [43],

$$g(\theta,s) = (\mathbf{R}f)(\theta,s) \tag{16}$$

together with its inverse transform [43],

$$f(x) = \frac{1}{4\pi^2} \int_{S^1} \int_{\mathbb{R}^1} \frac{\frac{\mathrm{d}}{\mathrm{d}s} g(\theta,s)}{x \cdot \theta - s} \mathrm{d}s\mathrm{d}\theta. \tag{17}$$

Here beams are modeled as straight lines $x \cdot \theta = s$, where $\theta \in S^1$ and $s \in \mathbb{R}^1$.

Then we can use the Fourier slice theorem [44],

$$(\mathbf{R}_\theta f)\hat{}(\sigma) = (2\pi)^{(n-1)/2} \hat{f}(\sigma\theta), \tag{18}$$

where $\sigma \in \mathbb{R}^1$. The $\hat{}$ stands for 1D Fourier transform. We include the Hilbert transform $\mathbf{H}$ [44],

$$(\mathbf{H}h)\hat{}(\sigma) = -i \, \mathrm{sgn}(\theta) \hat{h}(\sigma), \tag{19}$$

to acquire the FBP algorithm,

$$f = \frac{1}{2}(2\pi)^{1-n}\mathbf{R}^{\#}\mathbf{H}^{n-1}(\mathbf{R}f)^{(n-1)}, \tag{20}$$

where $\mathbf{R}^{\#}$ is the dual of the Radon transform.

Furthermore, the produced slices can be rendered into a 3D model (Fig. 12c), so as to represent the original 3D geometry. Reconstruction is usually done with a program provided by the µCT manufacturer, and can be saved as raw data in a 3D format or as a stack of images in any universal image file format. After reconstruction, user can transform image data to any software for further processing and structural analysis.

The scanning voxel size is a characteristic measure of the recorded image data and determines the best level of detail that can be resolved during the reconstruction [45]. To optimize the process of reconstructing, a tradeoff can be made between the reconstructed voxel size and computational requirements (memory and processor time).

4.1 Image colour depth

Scanning by µCT provides digital images like any related method. A single image can be dispersed into the number of colours used, i.e. the *colour depth*. For example,

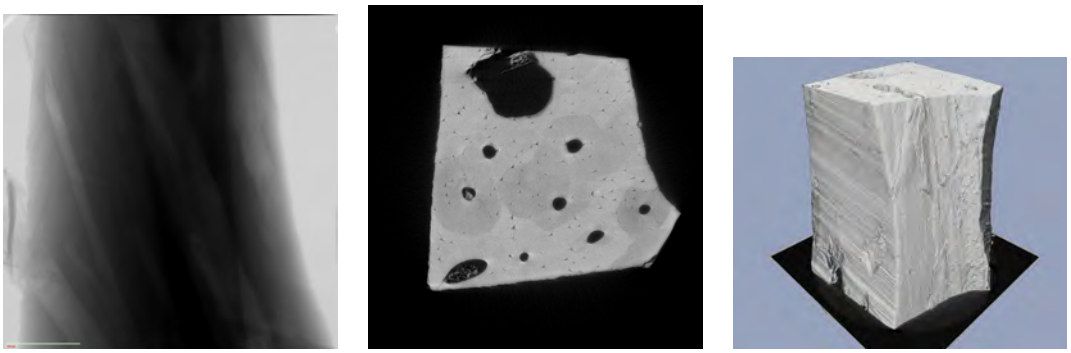

(a) (b) (c)

Figure 12. a) Micro-CT device saves projection images, i.e. shadowgrams, of the object. b) Projection images are reconstructed as transverse cross-sectional slices so the 3D volume can be analyzed. c) Whole 3D volume rendered as a 3D image. The black plane shows the location of the slice in b).

a common format for digital images is the JPEG, which in the gray-scale format contains a total of 256 shades. A definition for the colour range, or *dynamic range*, is the number of amplitude quantization levels such that [46]

$$L = 2^B, \tag{21}$$

where B represents the bit depth. The mentioned JPEG is thus an 8-bit image with given $2^8 = 256$ gray-scale tones. A related colour image has a depth of 24 bits with 16.7 million colours, represented by a combination of three 8-bit channels of red, green and blue (RGB). Colour depths and some applications used are shown in Table 5.

In a gray-scale image, a pixel with no information is represented by 0, and is typically visualized by black. If a photon hits a pixel, the latter contains information and is represented by a number higher than 0. Hit levels from 1 to 255 represent different shades of gray between black and white. The difference between a lower and higher colour depth is illustrated in Fig. 13. For a 1-bit image, the highest level is 1, corresponding typically to visualization by white.

In X-ray microtomographs, it is common to record data in a 16-bit format, although some older image processing software or image formats support only 8-bit images. Display hardware of computers affects the image quality shown to the eye. For instance, LCD displays typical in clinical use are able to show 12-bit channels while consumer displays are usually restricted to 8 bits [47]. Shades can always be downgraded by combining, though this process loses valuable data. By processing the image with appropriate software, we can either maintain maximal information recorded or compress the image by optimizing between the file size and image quality. A typical tomography scan can take several gigabytes of disk space and requires the same amount of RAM memory when processed. Powerful computers and large data storages are thereby needed to handle such image data.

4.2 Image defects

An image can never be regarded as a perfect representation of the original object. Whether the image is analogue or digital, gray-scale or colour, it always features some defects. These defects can efficiently be reduced by numerous possibilities of digital image processing. Tiny defects may not be visible if the picture is shrank to a smaller size or printed out. Troublesome the case is when the image is recorded with a high resolution sensor and shown in full scale, on a projector for example.

Table 5. Image types and the corresponding amounts of possible colours

Image type	Amount of colours	Application
1-bit	$2^1 = 2$	Binary
2-bit	$2^2 = 4$	CGA
4-bit	$2^4 = 16$	EGA
8-bit	$2^8 = 256$	VGA, gray-scale JPEG
12-bit	$2^{12} = 4{,}096$	
16-bit	$2^{16} = 65{,}536$	Clinical gray-scale
24-bit	$2^{24} = 16{,}777{,}216$	True colour
30-bit	$2^{30} \approx 1.073$ billion	HDMI
64-bit	$2^{64} \approx 1.885 \cdot 10^{19}$	Modern graphic cards

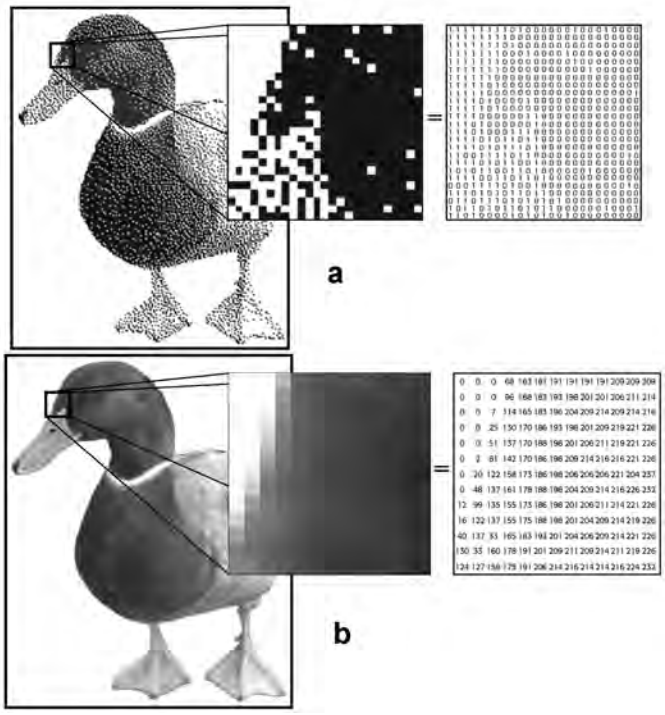

Figure 13. An a) 1-bit and an b) 8-bit image of the same object [40]. Notice the information of shades of gray stored in each pixel as numbers and how this affects the picture.

Some defects typical of µCT impact the image analysis and must therefore be reduced.

Noise is one of the most common disturbances in digital X-ray µCT images. It is analogous to grains in a film, and is common in digital sensors [40]. As a visual effect, noise can be a neat thing, but for clinical purposes noisy means inaccurate or even unreadable in the worst case. Digital sensors generate two different kinds of noise, *luminance noise*, which is also known as white or background noise, and *chrominance noise* which can include noisy patterns of changing luminance or bright speckles, or can appear as patterns of colours, usually wrong ones. Noise can be reduced to some extent, but it cannot be totally reduced. Noise cancellation algorithms and filters are part of almost every editing program. For the present study, noise reduction for the luminance noise was done by using a technique of background denoising. To this end, the background is considered more or less empty, and the gray-scale profile is corrected accordingly. The method of denoising used is illustrated in Fig. 14.

Sometimes unwanted objects or patterns may appear in the image due to defects in the CCD sensor or the lens. When during µCT scanning multiple images are taken from the same object at different angles, a few inactive pixels on the sensor can build up an effect which results in a ring artifact in the reconstructed µCT image (Fig. 15). A spot-like artifact can appear if multiple images are taken at the same angle, and the object is shaking a bit. When aligned, the faulty pixels sum up to a wider area. Usually either the operating software of the scanner or the reconstruction software have tools to reduce the ring artifacts.

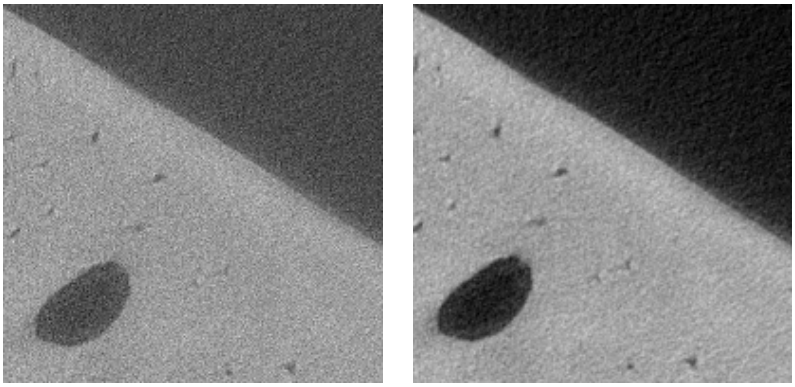

(a) (b)

Figure 14. Removing noise from images is most crucial for later analyses. A zoomed area of a slide from a sample (CTJ019) as a) original and b) filtered. Notice how the small detail and the boundary becomes more vivid.

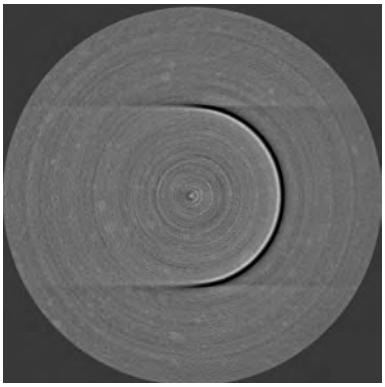

Figure 15. A ring artifact can be a result of faulty pixels in the CCD sensor. In this figure a bone phantom custom-made of epoxy resin and aluminium oxide was scanned over 180 degrees. As can be seen, a group of pixels have not recorded anything, for an unknown reason, and the artifact is spanned over the angle interval. Several smaller rings which are definitely not part of the actual composition of the phantom can also be seen.

During one exposure cycle an individual photosite can fill up from too many electrons [40]. Excessive electrons can then leak or overflow to adjacent photosites. This phenomenon is called *sensor blooming*, and can be detected as extra shadow figures around an object with high contrast lines. Sensor blooming looks just like chromatic aberration, the colourful halos around an object when different wavelengths do not focus on the same focal plane due to the varying refraction.

5 Materials and methods

5.1 Samples

The samples used comprise twenty-four (24) human cadaveric bone specimens of cortical bone from the proximal anterior shaft of adult human femora with a mean age of 48.7 (±16.3) (20 male with a mean age of 48 (±17.3) and 4 female with a mean age of 52.3 (±10.7)). Specimens were obtained by medical and forensic autopsies, conducted at Department for Pathology, Kuopio University Hospital. The ethical permission was granted by the National Authority for Medicolegal Affairs (TEO, 5783/04/044/07). Slices of cortical bone were cut below the minor trochanter (Fig. 16). Samples for µCT imaging were extracted with a drill or a band saw, and were approximately 1-5 mm in diameter and 7 mm in length. They were stored individually in a phosphate buffered saline (PBS) solution (pH = 7.4) and kept frozen at a temperature of -80 °C until preparation.

5.2 Sample preparation

The samples were dried in a freeze dryer Christ ALPHA 1-4 (Martin Christ, Osterode am Harz, Germany, (Fig. 17) which sublimated the ice. The device was connected to a vacuum pump (Edwards RV3 H.P., Edwards High Vacuum International, Crawley, West Sussex, UK) creating a 0.045 mbar vacuum inside the dryer chamber. The samples were cleaned of solid salts with compressed air and ground manually to fit the field of view (FOV) of the µCT device (diameter of the tip of the sample < 1.3 mm). To ease the scanning procedure, a glass capillary featured a sample holder, and samples were glued on the tip of this holder by epoxy based glue. In Fig. 18 a fully prepared bone sample can be seen.

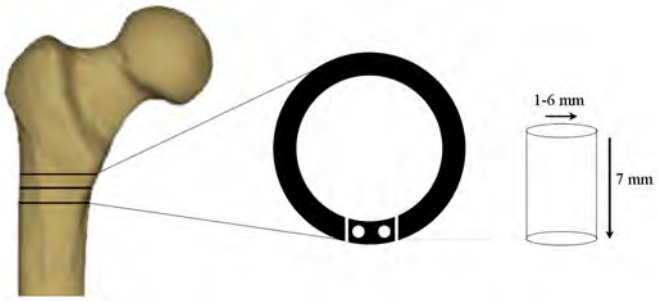

Figure 16. The samples for this study were cut from cortical bone slices of the proximal anterior shaft of human femora.

Figure 17. Christ Alpha 1-4 connected to a vacuum pump (on the left side) was used to remove water from samples preserved in PBS solution.

Figure 18. A fully prepared sample ready for scanning. It was defrosted, ground and glued to a glass capillary. Imaging was done of the small tip of the sample.

5.3 Micro-CT device

Micro-CT imaging was carried out using Xradia MicroXCT-400 (Xradia Inc., Concord, CA, USA, Fig. 19(a)). This device features an X-ray source of $20 - 90\,\mathrm{kV}$ (Fig. 19(b)). The device can be operated at power levels of $1-8\,\mathrm{W}$ [48]. The sample can be up to 500 mm in diameter, 400 mm in height and 15 kg in weight. During scanning the samples can be heated or cooled, pressurized, or their surroundings can be other than air (other gas or liquid in an X-ray transparent container). Also samples can be imaged under real operation conditions (current flowing through electrical components or mechanical parts in motion) or while subject to mechanical forces.

(a) (b)

Figure 19. a) Xradia MicroXCT-400 and its b) X-ray source ($20 - 90\,\mathrm{kV}$) (on the left), sample holder (in the middle) and optical lenses (on the right).

5.4 Micro-CT scanning

Each scanning consists of at least 1800 shadowgrams in an angle interval of 184 degrees. An exposure time of 60 or 100 seconds was used and the power (between 2.5 and 8 W) and voltage (25 to 90 kV) combination was set based on the exposure time. As a safety precaution, power and voltage was set so that current never exceeded 100 µA. For all the samples a lens with a magnification of 20X was used. Distance between the sample and source (S_0) was 20 to 35 mm, and the distance between the sample and detector ($S_1 - S_0$) was usually 4 or 5 mm, depending on the size of the sample. Guidelines for these distances were that the former would be about 5 to 7 times the latter. Samples were located as close to the detector as possible still with some room for it to spin around its long axis. For each sample the scanning took about 60 hours to complete.

The scanning procedure is dependent on the sample properties. Although every sample was materially the same and about the same size with a cross section

diameter of 1 mm, each sample had to be specified independently. The cross section of the sample perpendicular to the long axis was fitted fully inside the device's field of view (FOV, Fig. 20(a)) which was 1.3 mm in diameter for the used magnification of 20X. Otherwise the spinning of the excessive part would have disturbed the final result. Distances S_0 and $(S_1 - S_0)$ were partly chosen with this in mind. As for the filter used, some of the thinnest glass filters (LE1, LE2 or LE3) were used from a series of filters provided by the manufacturer (Fig. 20(b)). Filters and dimensions of the object had an effect on the image brightness so that power output of the device had to be optimized for each sample for the best possible result. A guide distributed by the manufacturer was used to choose correct filter and power levels. Software used for operating the Xradia MicroXCT-400 was MicroXCT 7.0.2817. Scanning was performed at atmospheric pressure and normal room temperature (22 °C).

Some single scans were taken before the actual imaging to be sure the results would be desirable. With these the filter used during scanning was also determined by separating the background from the object and optimizing the used bit depth. It was to be made sure that some radiation came through the object in every part but also that the background was not overexposed (photon limit was not reached for any pixel).

5.5 Image post processing

3D bone volumes were reconstructed from the through transmission images with Xradia Reconstructor 7.0.2817. This software was delivered by the manufacturer and is designed to control the produced images.

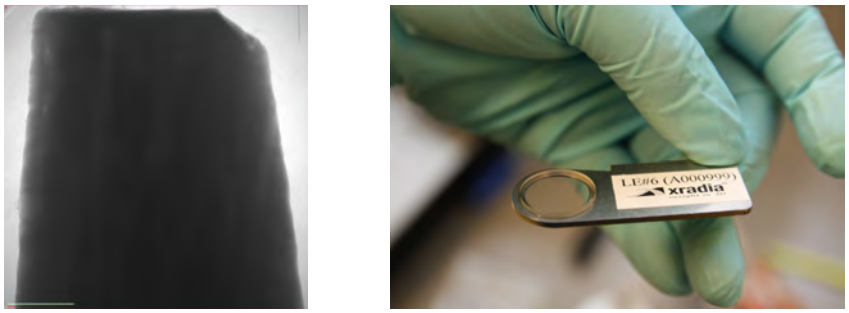

(a) (b)

Figure 20. a) A single absorption image of the tip of a bone sample (CTJ022) imaged with 20X magnification. This image operates as the FOV at the same time and includes fully the cross section parallel to the long axis. b) A filter used in the imaging sequence to flatten out the lower part of the energy spectrum.

Reconstructed images, or slices, were oriented perpendiculary to the long axis of the imaged object and numbered from bottom to the top. Also, some enhancements were performed in this phase. Image sharpening was done with pixel center shifting (Fig. 21) and roughness due to the hard and dense material was corrected with a standard beam hardening correction (Fig. 22). Ring artifacts were removed by using 3-section high contrast ring removal. Also a filter was used based on the Shepp-Logan function.

Finished 16-bit reconstructions were operated in image processing software ImageJ 1.40c (National Institutes of Health, Bethesda, MD, USA). Image background noise was removed by using a custom made 3D variance filter.

Some of the samples were remodeled with Avizo 7.0.0 Fire Edition (Visualization Sciences Group SAS, Burlington, MA, USA) for better visualizations.

5.6 Analysis of bone micro-architecture

Parameters of bone micro-architecture (i.e. morphological parameters of bone) were determined by software CTAn (version 1.11.4.2, Skyscan™, Kontich, Belgium). Data were imported into the software as 8-bit bitmaps, and a region of interest (ROI) was selected. A polygonal boundary was drawn inside sample boundaries according to the thinnest part of the sample. Image noise at the bottom and known ring artifacts at the top of the images were the most crucial limiting factors for the height of ROI. Number of slides and the geometry of ROI was chosen with the maximum volume and maximum image quality in sight. Typical dimensions for the ROIs were 600-900 µm in diameter and 500-930 µm in height. Morphological parameters were determined for each sample inside the selected ROI.

Several different morphological parameters can be obtained from the reconstructed bone volume. The parameters were determined directly in 3D inside a surface-rendered volume model [49]. Tissue volume (TV) and bone volume (BV) were based on the separation of bone voxels and empty voxels inside the ROI which was fully set inside the scanned bone sample boundaries. TV refers to any kind of tissue independent of its density and BV accounts for the binarized solid volume.

Let us call the bone volume fraction as $\frac{BV}{TV} = P_P$ and the trabecular number (Tb.N) as $Tb.N = P_L$. Trabecular thickness (Tb.Th), trabecular separation (Tb.Sp) and bone surface to bone volume ratio ($\frac{BS}{BV}$) can then be defined as [45]:

$$Tb.Th = \frac{P_P}{P_L} = \frac{BV}{TV \cdot Tb.N} \tag{22}$$

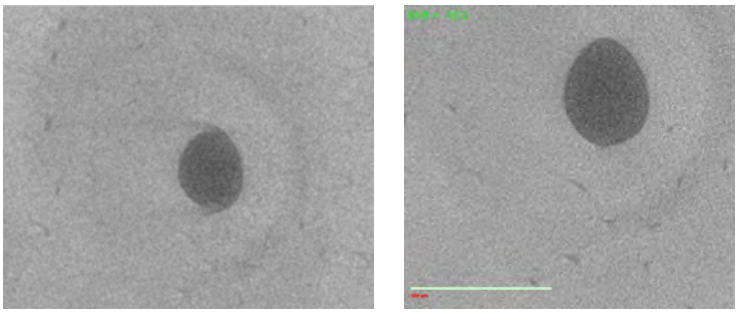

(a) (b)

Figure 21. a) Original absorption images were a little bit out of focus and would have lead to inaccurate reconstruction. (b) With the center shift function the geometry of surfaces was corrected.

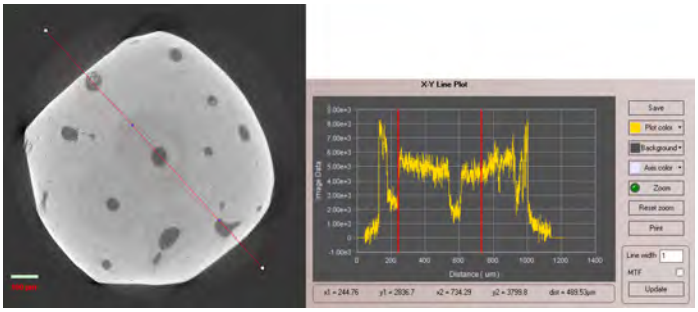

(a)

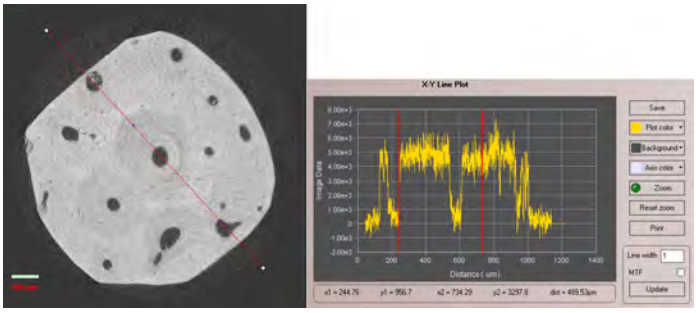

(b)

Figure 22. a) Edge of the sample seems denser and the density profile is inhomogeneous. b) The Beam hardening constant was set to equalize the distribution of matter across the sample and to homogenize the density profile across the entire cross section of the sample.

$$Tb.Sp = \frac{1 - P_P}{P_L} = \frac{1 - \frac{BV}{TV}}{Tb.N} \tag{23}$$

$$\frac{BS}{BV} = \frac{2 \cdot P_L}{P_P} = \frac{2 \cdot Tb.N \cdot TV}{BV}. \tag{24}$$

From these equations we obtain a definition for the trabecular number [45, 49],

$$Tb.N = \frac{1}{(Tb.Th + Tb.Sp)}. \tag{25}$$

The degree of anisotropy (DA) can be defined such that

$$DA = \left(1 - \left[\frac{\min\ eigenvalue}{\max\ eigenvalue}\right]\right), \tag{26}$$

where DA is 0 for total isotropy and 1 for total anisotropy. DA was tested with a mean intercept length analysis where a grid of test lines was distributed inside the binarized volume in a large number of different 3D angles. DA was determined from the line length to tissue volume ratio by calculating the number of intersections the lines have [49].

The structure model index, SMI, is given by

$$SMI = 6 \cdot \left(\frac{S' \cdot V}{S^2}\right), \tag{27}$$

where S is the object surface area before dilation, S' is the change in surface area caused by dilation, and V is the initial object volume. SMI indicates the relative commonness of rods and plates in a structure involving a measurement of surface convexity.

For any data set $x_i (i = 1, \ldots, n)$, arithmetic mean (μ) was determined by

$$\mu = \frac{1}{n} \sum_{i=1}^{n} x_i. \tag{28}$$

The standard deviation (SD) of a data set is given by

$$SD = \sqrt{\frac{\sum_{i=1}^{n} (x_i - \mu)^2}{(n-1)}}. \tag{29}$$

Finally the coefficient of variation (CV) is defined by

$$CV = \frac{SD}{\mu}. \tag{30}$$

Calculations were done with built-in 3D morphometric analysis of CTAn including all of the parameters available. Although the program is originally designed to examine trabecular bone, with proper thresholding the definitions of gray-scale can be inverted and the same analysis can be applied to cortical bone [50]. The nomenclature is modified to characterize the features of cortical bone (Table 6) [50, 51].

Canal and lacunae volume feature the empty space inside the tissue volume. Surface was measured as the interface of dense material and the empty space enclosed by the Haversian canals and lacunae. As the canal (and lacuna) diameter we used the mean diameter of the canals (and lacunae). Canal separation was the mean distance that separated the canals within the canal network, and canal number was

Table 6. The morphological parameters used in this study [50, 51].

Trabecular bone	Abbrv.	Cortical bone	Abbrv.
Tissue volume	TV	Tissue volume	TV
Bone volume	BV	Pore volume	V
Bone surface	BS	Pore surface	S
Bone volume fraction	BV/TV	Cortical porosity	V/TV
Bone surface to tissue volume	BS/TV	Cortical surface to tissue volume	S/TV
Trabecular thickness	Tb.Th	Pore diameter	Dm
Trabecular separation	Tb.Sp	Pore separation	Sp
Trabecular number	Tb.N	Pore number	N
Structure model index	SMI	Structure model index	SMI
Degree of anisotropy	DA	Degree of anisotropy	DA

the mean number of canals per micrometer. The structural model index indicated the relative prevalence of rods and plates in the structure.

For the analysis of micro-architecture, the bone volumes were segmented by thresholding (Fig. 23). In a segmented image, voxels with levels of linear attenuation lower than the threshold represented empty space (bright areas), while voxels with levels higher than this represented bone (dark areas). Haversian canals and lacunae were thus separated from bone tissue. The threshold level was chosen individually for each sample due to sample-specific variations in image attributes such as brightness. This level was determined visually by maximizing the amount of details and minimizing noise. The original 16-bit images were used as references for the amount of details.

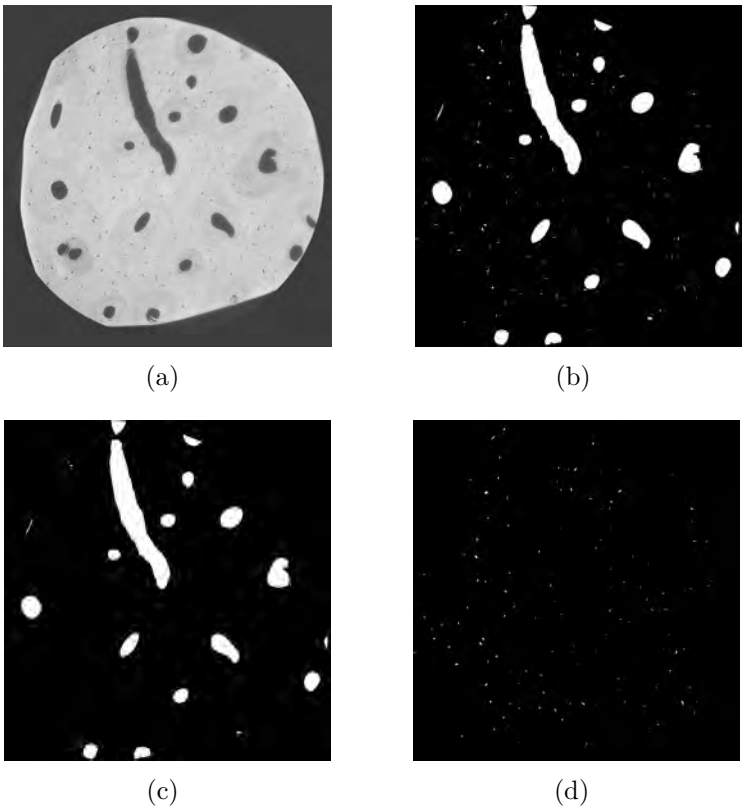

Figure 23. a) An original 16-bit slide used for comparison for the level of detail. b) Image was thresholded for the data analysis. First set included both Haversian canals and lacunae (Co). c) Haversian canals (Ca) were separated, analyzed and subtracted from the data set. d) After removing the Haversian canals an analysis was done of lacunae (Lc) only. Tissue volume was corrected in the final analysis.

Three versions of images per each sample were created: one including both the canals and lacunae (abbreviated by Co as combined), one including only the Haversian canals (abbreviated by Ca) and the last one with only the lacunae (abbreviated by Lc). In the two latter cases the canal or lacunae volume, determined from image histograms, was subtracted from the tissue volume so as to remove the bias caused by the canals (lacunae). Abbreviations are used as prefixes in the results for individual data sets.

Pearson's correlation coefficients were calculated between the morphological parameters acquired for the samples. This was done using IBM SPSS Statistics (version 20, IBM Corporation, New York, NY, USA). A correlation was considered statistically significant when its p-value was less than 0.05. Diagrams showing linear correlation (R^2 coefficient, which is the Pearson's coefficient squared) between cortical porosity and other parameters were drawn with Matlab (The MathWorks, Inc., Natick, MA, USA).

6 Results

6.1 Effects of sample specific scanning and thresholding parameters

The impact of scanning and thresholding parameters, individually tuned for each sample, on bone morphological parameters is demonstrated for one bone sample. For this evaluation the same sample was imaged with two different settings which represent an extreme range of scanning parameters for the whole sample set studied. The region of interest (ROI) was chosen as cylindrical and was placed as identical as possible in the two cases. It is evident from Table 7 that the values of morphological parameters determined differ by approximately 4 % between the two trial scans. The resulting effect is small compared to inter-sample variability in these morphological properties.

Choice of the threshold level was seen to have a tremendous effect on the image quality. A level too small lead to images with less detail whereas too high a level resulted in noise affecting the analyzed volume. The mean value of the threshold levels was 165 ($\pm$ 14 with a range of 144-192). To show how much the amount of details vary depending on the selection of the threshold level, in Figure 24 we show results one sample that was analyzed with three threshold values chosen from the threshold level distribution for the samples: the mean value and the mean value $\pm$ SD.

Table 7. Scanning parameters, threshold levels and resulting morphological properties for one bone sample featuring a case example on the impact of the choice of the scanning parameters.

Scanner parameter	Unit	Scan 1	Scan 2	Difference (%)	
Output voltage	kV	90	30		
Power	W	8	3		
Filter used		LE2	LE2		
Number of images taken		1800	1850		
Exposure time	s	60	100		
Sample distance from source	mm	25	35		
Sample distance from detector	mm	4	5		
Pixel size	µm	0.58	0.59	0.01	(1.7)
Upper threshold limit		167	163	-4.0	(-2.4)
Morpological parameters	**Abbr.**	**Scan 1**	**Scan 2**	**Difference (%)**	
Tissue volume	TV	391718749	398220217	6501468	(1.6)
Combined cortical porosity	Co.V/TV	5.13	4.95	-0.18	(-3.6)
Combined pore diameter	Co.Dm	48.6	46.8	-1.82	(-3.8)
Combined pore number	Co.N	0.00105	0.00106	0.00001	(0.9)
Combined pore separation	Co.Sp	48.39	48.98	0.59	(1.2)
Degree of anisotropy	DA	0.56	0.57	0.01	(1.5)
Structure model index	SMI	8.62	7.60	-1.02	(-12.5)

In addition, the same sample was thresholded and the bone parameters determined for several different threshold levels. Besides the level used for this sample in the actual analysis, four different levels were used: two lower and two higher ones with a level increment of 2 units. In this case the tested levels were 159, 161, 163, 165 and 167, and the results are shown in Table 8. Canals were subtracted from the images, and the data included only the lacunae.

Due to the choice of the threshold level, the coefficient of variation was about 0.10 for the morphological parameters. This corresponded to a 10 % error for the chosen levels. For the same set the total volume of the lacunae varied more than 50 %. In Fig. 25 we show a magnified part of a cross section for all of the used threshold levels so as to illustrate their effect on the level of detected details, while the variation in the amount of noise related to the choice of the threshold level is illustrated in Fig. 26.

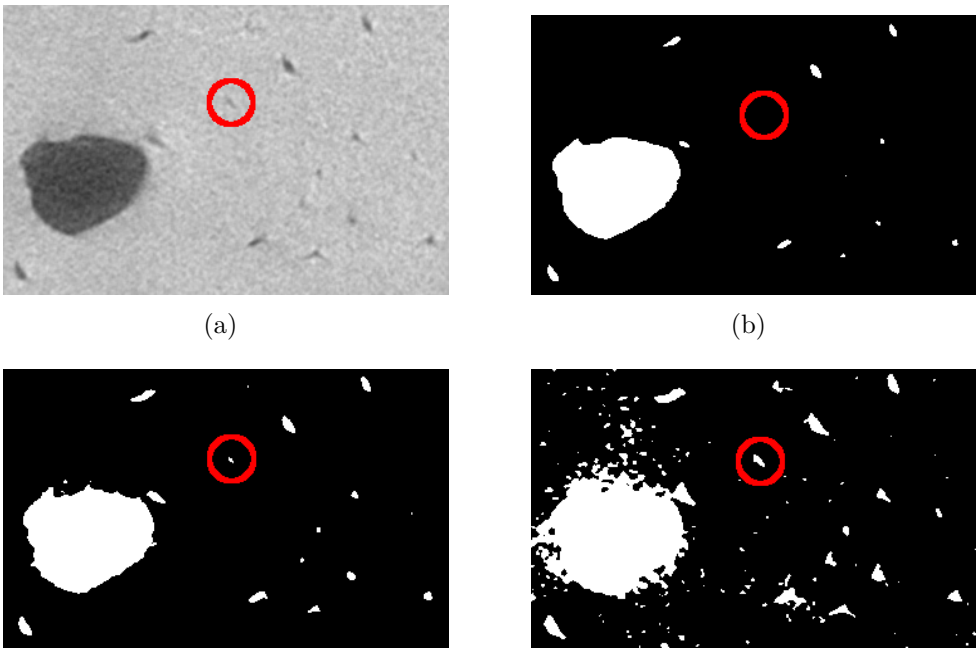

Figure 24. a) A zoomed-in area from the original 16-bit slide of the sample used for comparison of segmented images. b) The result of using a threshold level of 151, i.e. one SD lower than the mean threshold level of all the samples. c) The result of using a mean threshold level of 165. d) The result of using a threshold level of 179, i.e. one SD higher than the mean threshold level. As can be seen (marked with red circle), a detail clearly visible in the original image does not show up with too low a threshold level (b). The mean value appears to be almost the correct value for this sample although the boundary of the Haversian canal is not as smooth as it should be. For an SD value of 14 this is a coincidence. For a too high threshold level noise starts to limit the image quality (d).

An automated determination of the threshold level was tested for one sample by ImageJ. The sample volume was loaded into the program and the automatic thresholding tool was used for the whole stack at once. Some examples are shown in Fig. 27, and it is evident that this method did not provide the expected amount of details while some amount of noise was left in the segmented image. In Table 9 we show the threshold values given by the automatic thresholding tools of ImageJ. Based on these results, the threshold level should best be located somewhere on the uprising slope of the gray-scale histogram when determined by visual inspection.

Table 8. The effect of threshold value was tested for one sample with a varying threshold value.

Sample	Upper threshold limit	Tissue volume TV $10^{-3}\cdot$ mm^3	Lacuna volume Lc.V $10^{-3}\cdot$ mm^3	Cortical porosity Lc.V/TV %	Lacuna diameter Lc.Dm µm	Lacuna number Lc.N $1/\mu$m	Lacuna separation Lc.Sp µm	Degree of anisotropy Lc.DA	Structure model index Lc.SMI
CTJ019	159	516.5	3.94	0.76	3.90	0.0019	52.7	0.71	2.80
	161	516.5	4.26	0.82	3.96	0.0020	52.0	0.65	2.86
	163	516.5	4.57	0.89	4.02	0.0021	51.2	0.64	2.93
	165	516.5	4.90	0.95	4.08	0.0022	50.4	0.62	3.01
	167	516.5	5.23	1.01	4.13	0.0023	49.5	0.62	3.13
Mean		516.5	4.58	0.89	4.02	0.0021	51.2	0.65	2.95
SD		0.00	0.51	0.10	0.09	0.0002	1.3	0.04	0.13
CV		0.00	0.11	0.11	0.02	0.09	0.03	0.06	0.04

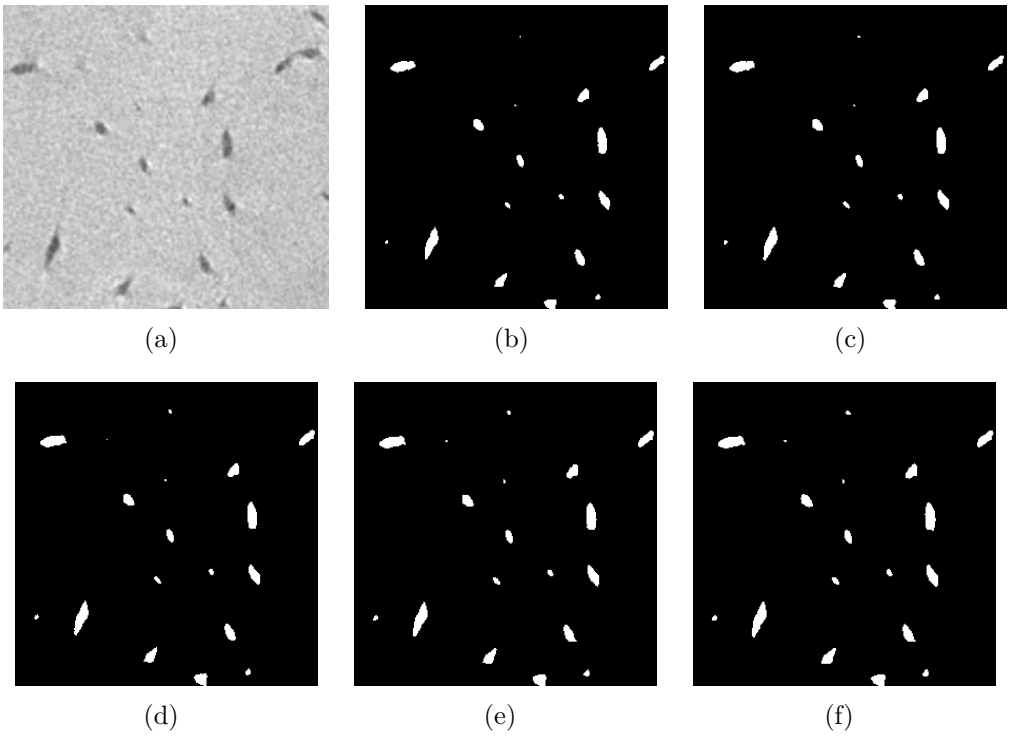

Figure 25. A small portion of a cross section of the image is zoomed-in from a) the original 16-bit image and from those resulting from using a threshold level value of b) 159, c) 161, d) 163, e) 165 and f) 167. Note the change in the amount of details of the size of the smallest lacunae when the threshold value changes from its lowest level to the highest.

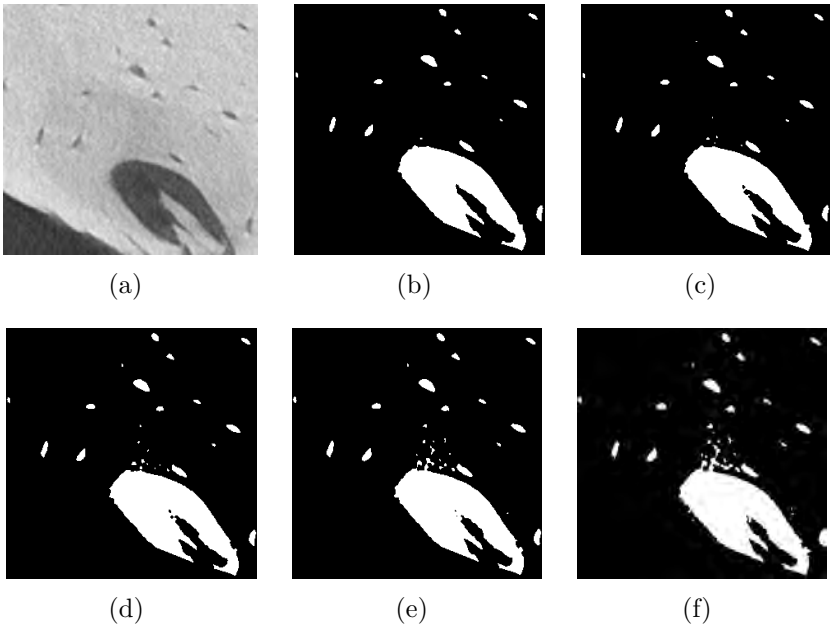

Figure 26. A small portion of a cross section of the image is zoomed-in from a) the original 16-bit image and from those resulting from using a threshold level value of b) 159, c) 161, d) 163, e) 165 and f) 167. Note the change in the amount of noise when the threshold value changes from its lowest level to the highest.

Table 9. Automatic thresholding tools in ImageJ were used for one sample. The resulting threshold levels varied a lot and were typically quite different from the one acquired by visual inspection.

ImageJ method	Level value
Default	145
Huang	134
Intermodes	142
IsoData	99
IJ_IsoData	145
Li	136
Mean	180
MinError	-
Minimum	145
Moments	172
Otsu	145
Percentile	201
RenyiEntropy	181
Shanbhag	107
Triangle	173
Yen	184
Visual inspection	167

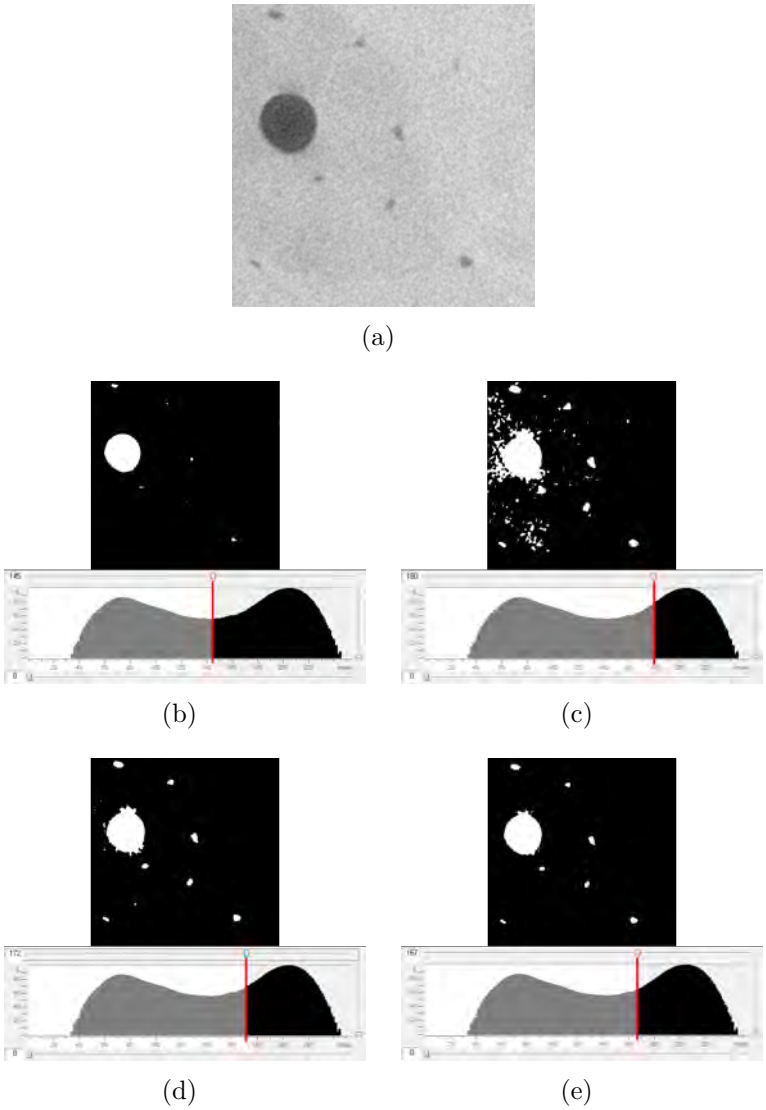

Figure 27. A few examples of the results of using automatic image thresholding tools for one of the samples. a) The original 16-bit slide used for comparison, b) the result of using the automatic thresholding tool the "default" method which gave 145 for the threshold level, c) the result of using the automatic thresholding tool the "MaxEntropy" method which gave 180 for the threshold level, d) the result of using the automatic thresholding tool the "Moments" method which gave 172 for the threshold level, e) thresholded image and the threshold level acquired visually by optimizing between detail and noise. The red line in the histograms marks the value of the threshold level. Notice that, in panel (e) the optimal threshold value is not at the saddle point of the diagram.

6.2 Statistical analysis

Morphological parameters for the data set of combined porosity are shown in Table 10. Data consisting only of canals are shown in Table 11 and those of lacunae in Table 12.

Correlations between the acquired morphological parameters are summarized in Tables 13, 14 and 15.

Distribution of cortical porosity across the samples is shown in Fig. 28 Throughout the set most of the samples had a porosity of 4 to 8 % including Haversian canals, and of 0.2 to 0.5 % with lacunae only.

Cortical porosity was correlated with some of the morphological parameters. A strong correlation occured between the pore diameter and combined porosity ($r^2 = 0.64$, $p < 0.001$) and canal porosity ($r^2 = 0.60$, $p < 0.001$) (Fig. 29), but for the data set including only the lacunae the correlation was not as clear.

Lacuna number (Lc.N) had a clear linear correlation with cortical porosity ($r^2 = 0.97$, $p < 0.001$). For the data set including both Haversian canals and lacunae or canals alone the correlation was not as clear due to the changing size of the canals ($r^2 = 0.17$, $p > 0.05$ and $r^2 = 0.29$, $p > 0.01$ respectively, Fig. 30).

Pore separation was correlated slightly with the combined cortical porosity and lacunae porosity, as is evident from Fig. 31. For lacunae the correlation was negative ($r^2 = 0.35$, $p < 0.01$).

Degree of anisotropy was not correlated with cortical porosity (Fig. 32).

Structural model index (SMI) seemed to be correlated with the combined cortical porosity (Co.V/TV) ($r^2 = 0.48$, $p < 0.001$) (Fig. 33), but not with the canal porosity (Ca.V/TV) or lacunae porosity (Lc.V/TV).

Morphological parameters were measured at University of Eastern Finland (Kuopio) with a different device (Skyscan 1172, Skyscan Artselaar, Belgium) and imaging setup. Comparisons of distributions of morphological data by Xradia (Xr) and SkyScan (SS) are shown in Fig. 34. For the cortical porosity, pore diameter and pore separation the Xr Ca set was most consistent with the SS data. The Co data set had similarities with the SS data for the porosity and pore diameter. When considering the Lc data set of the Xradia and the SS data, similar results for pore number, DA and SMI were measured.

Table 10. Morphological parameters measured for 24 bone samples. The results are for total VOI including the Haversian canals and lacunae combined.

Sample	Combined sample volume Co.TV [$10^{-3}\cdot$ mm^3]	Combined pore volume Co.V [$10^{-3}\cdot$ mm^3]	Combined cortical porosity Co.V/TV [%]	Combined pore diameter Co.Dm [µm]	Combined number of pores Co.N [1/µm]	Combined pore separation Co.Sp [µm]	Combined degree of anisotropy Co.DA	Combined structure model index Co.SMI
CTJ001	313.0	22.80	7.28	42.5	0.0017	58.8	0.77	7.14
CTJ002	628.3	40.69	6.48	37.3	0.0017	59.9	0.47	7.34
CTJ003	381.0	62.19	16.33	83.5	0.0020	59.9	0.70	12.78
CTJ004	597.5	33.48	5.60	41.4	0.0014	61.3	0.64	10.33
CTJ005	453.9	65.08	14.34	56.9	0.0025	53.3	0.58	7.44
CTJ006	130.9	7.75	5.92	35.6	0.0017	56.2	0.84	7.84
CTJ007	524.9	115.11	21.93	110.9	0.0020	67.2	0.70	18.20
CTJ008	358.0	13.55	3.79	30.6	0.0012	59.4	0.75	7.26
CTJ009	344.0	22.47	6.53	43.7	0.0015	54.3	0.73	9.31
CTJ010	342.4	14.69	4.29	38.1	0.0011	56.4	0.56	8.05
CTJ011	662.3	46.48	7.02	33.9	0.0021	55.1	0.79	6.30
CTJ012	305.6	45.62	14.93	48.8	0.0031	55.1	0.57	11.15
CTJ013	464.8	35.21	7.57	55.5	0.0014	54.9	0.94	8.33
CTJ014	246.1	16.31	6.63	26.2	0.0025	49.5	0.53	7.54
CTJ015	193.3	8.08	4.18	27.5	0.0015	53.7	0.76	9.07
CTJ016	404.8	23.49	5.80	36.8	0.0016	53.4	0.65	7.40
CTJ017	382.2	27.46	7.18	43.4	0.0017	51.5	0.78	9.31
CTJ018	627.3	39.13	6.24	46.5	0.0013	51.1	0.58	12.31
CTJ019	543.1	31.42	5.79	44.2	0.0013	47.8	0.60	8.16
CTJ020	156.2	7.71	4.94	17.9	0.0028	48.3	0.57	4.02
CTJ021	516.0	38.30	7.42	48.6	0.0015	58.7	0.72	11.42
CTJ022	445.6	19.61	4.40	39.2	0.0011	55.9	0.59	9.99
CTJ023	497.5	27.44	5.51	55.3	0.0010	53.5	0.65	10.88
CTJ024	311.0	44.48	14.30	128.5	0.0011	53.5	0.59	16.86
Mean	409.6	33.69	8.10	48.9	0.0017	55.4	0.67	9.52
SD	148.8	23.46	4.65	25.4	0.0006	4.4	0.11	3.19
CV	0.36	0.70	0.57	0.52	0.32	0.08	0.17	0.34

Table 11. Morphological parameters for 24 bone samples. These results are for bone volumes which include the Haversian canals but not lacunae. The lacunae were subtracted from the total tissue volume.

Sample	Canal sample volume Ca.TV [$10^{-3}\cdot$ mm^3]	Canal volume Ca.V [$10^{-3}\cdot$ mm^3]	Canal contribution to cortical porosity Ca.V/TV [%]	Canal diameter Ca.Dm [µm]	Canal number Ca.N [1/µm]	Canal separation Ca.Sp [µm]	Canal contribution to degree of anisotropy Ca.DA	Canal contribution to structure model index Ca.SMI
CTJ001	365.8	24.15	6.60	41.0	0.0016	186.4	0.83	2.94
CTJ002	627.2	39.60	6.31	38.0	0.0017	191.3	0.57	1.53
CTJ003	380.0	61.44	16.17	84.6	0.0019	189.5	0.73	0.25
CTJ004	595.9	32.01	5.37	42.9	0.0013	228.4	0.78	2.45
CTJ005	452.8	64.15	14.17	57.6	0.0025	147.5	0.60	3.17
CTJ006	130.5	7.30	5.59	37.4	0.0015	191.1	0.97	2.05
CTJ007	524.2	114.54	21.85	111.4	0.0020	210.0	0.73	4.40
CTJ008	356.7	12.26	3.44	33.0	0.0010	191.2	0.84	3.03
CTJ009	342.5	20.99	6.13	46.2	0.0013	229.2	0.69	0.79
CTJ010	340.9	13.25	3.89	41.3	0.0009	252.8	0.41	1.63
CTJ011	660.1	44.39	6.72	35.1	0.0019	218.1	0.84	1.84
CTJ012	304.6	44.73	14.68	49.6	0.0030	179.3	0.70	2.47
CTJ013	463.0	33.44	7.22	58.1	0.0012	229.4	0.92	−0.97
CTJ014	244.9	15.18	6.20	27.6	0.0022	164.0	0.62	2.82
CTJ015	192.7	7.46	3.87	29.1	0.0013	196.4	0.76	3.79
CTJ016	403.0	21.66	5.37	39.4	0.0014	244.2	0.73	1.68
CTJ017	380.2	25.49	6.70	46.0	0.0015	218.2	0.77	2.13
CTJ018	625.3	37.19	5.95	48.4	0.0012	232.4	0.61	3.98
CTJ019	538.8	26.63	4.94	49.7	0.0010	319.5	0.65	4.44
CTJ020	155.1	6.60	4.26	20.0	0.0021	149.6	0.90	1.02
CTJ021	514.6	36.93	7.18	50.0	0.0014	207.1	0.68	3.35
CTJ022	443.7	17.68	3.98	42.6	0.0009	247.4	0.69	3.46
CTJ023	495.0	24.91	5.03	59.8	0.0008	244.7	0.76	3.75
CTJ024	309.7	43.16	13.93	131.6	0.0011	195.3	0.58	3.13
Mean	410.3	32.30	7.73	50.8	0.0015	211.0	0.72	2.46
SD	147.3	23.55	4.74	25.4	0.0005	37.5	0.13	1.34
CV	0.36	0.73	0.61	0.50	0.35	0.18	0.17	0.54

Table 12. Morphological parameters measured for 24 bone samples. These results are for bone volumes which include the lacunae but not Haversian canals. The canals were subtracted from the total tissue volume.

Sample	Lacuna sample volume Lc.TV [$10^{-3}\cdot$ mm^3]	Lacuna volume Lc.V [$10^{-3}\cdot$ mm^3]	Lacuna contribution to cortical porosity Lc.V/TV [%]	Lacuna diameter Lc.Dm [µm]	Lacuna number Lc.N [1/µm]	Lacuna separation Lc.Sp [µm]	Lacuna contribution to degree of anisotropy Lc.DA	Lacuna contribution to tructure model index Lc.SMI
CTJ001	288.4	1.03	0.36	3.55	0.0009	68.6	0.69	3.08
CTJ002	588.7	1.08	0.18	3.26	0.0005	69.3	0.57	3.12
CTJ003	319.4	0.94	0.30	3.88	0.0006	83.9	0.67	2.95
CTJ004	565.4	1.48	0.26	3.54	0.0007	69.0	0.57	2.92
CTJ005	389.6	1.00	0.26	3.50	0.0006	67.8	0.28	3.57
CTJ006	123.7	0.47	0.38	3.79	0.0010	61.8	0.55	3.01
CTJ007	410.3	0.64	0.16	3.61	0.0003	103.8	0.66	3.33
CTJ008	345.7	1.29	0.37	3.57	0.0010	65.4	0.68	2.71
CTJ009	323.0	1.50	0.46	3.81	0.0011	62.5	0.63	2.81
CTJ010	329.2	1.45	0.44	3.96	0.0011	59.9	0.62	2.90
CTJ011	617.9	2.09	0.34	3.56	0.0009	59.9	0.60	3.46
CTJ012	260.8	0.88	0.34	3.37	0.0009	61.7	0.44	3.93
CTJ013	431.4	1.77	0.41	3.77	0.0010	62.1	0.64	2.91
CTJ014	230.8	1.12	0.49	3.57	0.0013	55.0	0.63	3.33
CTJ015	185.8	0.60	0.32	3.37	0.0009	54.7	0.91	3.55
CTJ016	383.1	1.83	0.48	4.01	0.0011	57.9	0.67	3.16
CTJ017	356.7	1.98	0.55	3.90	0.0013	56.3	0.77	2.81
CTJ018	590.0	1.95	0.33	3.59	0.0009	56.1	0.63	3.29
CTJ019	516.5	4.57	0.89	4.02	0.0021	51.2	0.64	2.93
CTJ020	149.6	1.14	0.76	4.40	0.0017	54.4	0.34	3.02
CTJ021	479.0	1.37	0.29	3.61	0.0007	64.9	0.80	2.97
CTJ022	427.6	1.93	0.45	4.30	0.0010	59.0	0.58	3.28
CTJ023	472.6	2.52	0.53	4.22	0.0012	58.8	0.57	3.02
CTJ024	267.8	1.30	0.48	3.56	0.0012	76.4	0.56	2.65
Mean	377.2	1.50	0.41	3.74	0.0010	64.2	0.61	3.11
SD	139.3	0.83	0.16	0.30	0.0004	11.2	0.13	0.30
CV	0.37	0.56	0.40	0.08	0.36	0.18	0.21	0.10

Table 13. Pearson's correlations between the morphological parameters of the combined data including the Haversian canals and lacunae. Significance of correlation: *p < 0.05, **p < 0.01, ***p < 0.001 and 'ns.' means not significant.

	Co.Dm	Co.N	Co.Sp	Co.DA	Co.SMI
Co.V/TV	0.802***	0.414*	0.426*	ns.	0.692***
Co.Dm		ns.	0.377	ns.	0.873***
Co.N			ns.	ns.	ns.
Co.Sp				ns.	0.439*
Co.DA					ns.

Table 14. Pearson's correlations between the morphological parameters for the data with Haversian canals only. Significance of correlation: *p < 0.05, **p < 0.01, ***p < 0.001 and 'ns.' means not significant.

	Ca.Dm	Ca.N	Ca.Sp	Ca.DA	Ca.SMI
Ca.V/TV	0,777***	0,542**	ns.	ns.	ns.
Ca.Dm		ns.	ns.	ns.	ns.
Ca.N			-0,688***	ns.	ns.
Ca.Sp				ns.	ns.
Ca.DA					ns.

Table 15. Pearson's correlations between the morphological parameters for the data with lacunae only. Significance of correlation: *p < 0.05, **p < 0.01, ***p < 0.001 and 'ns.' means not significant.

	Lc.Dm	Lc.N	Lc.Sp	Lc.DA	Lc.SMI
Lc.V/TV	0,689***	0,981***	-0,590**	ns.	ns.
Lc.Dm		0,570**	ns.	ns.	ns.
Lc.N			-0,670***	ns.	ns.
Lc.Sp				ns.	ns.
Lc.DA					ns.

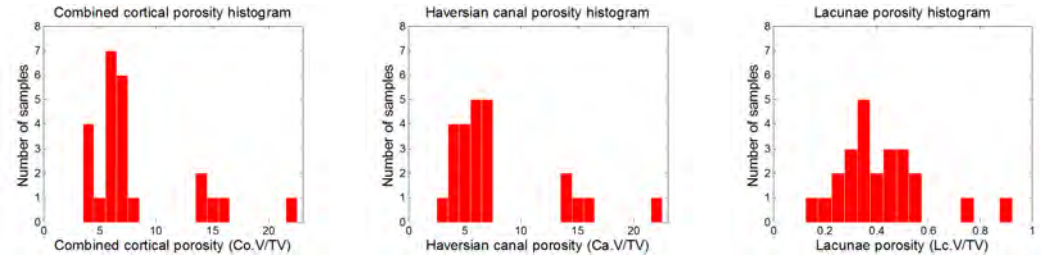

(a) (b) (c)

Figure 28. Distribution of cortical porosity of the samples a) including Haversian canals and lacunae combined, b) including only the Haversian canals and c) including lacunae only.

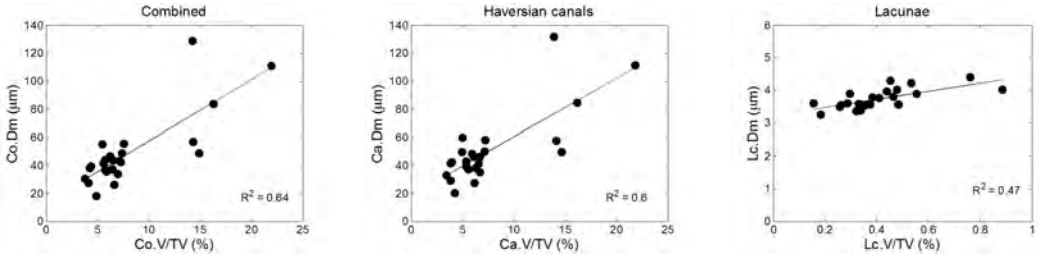

(a) (b) (c)

Figure 29. a) Pore diameter of the combined data (Co.Dm) and b) canal diameter (Ca.Dm) has a positive correlation with porosity. c) For lacunae diameter (Lc.Dm) this relation is not as strong.

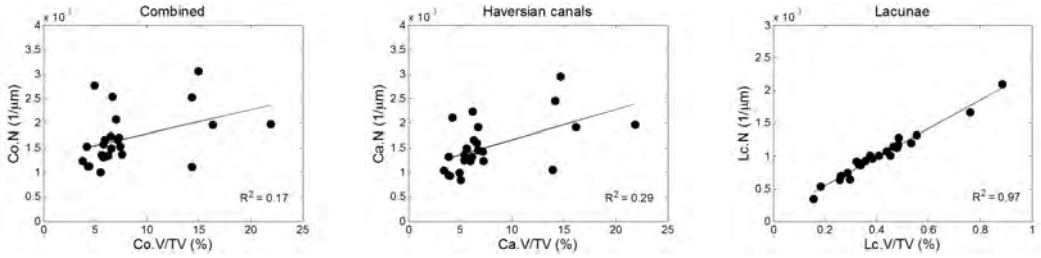

(a) (b) (c)

Figure 30. Pore number of the a) combined data set (Co.N) or b) canal data set (Ca.N) does not seem to be in correlation with porosity as much as with c) the lacuna number (Lc.N).

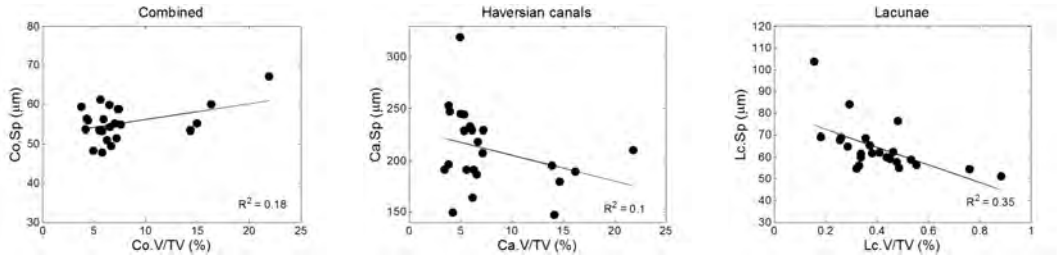

(a) (b) (c)

Figure 31. a) Combined pore separation had a slight positive correlation with the cortical porosity. b) For canal separation (Ca.Sp) correlation with porosity was not seen. c) Lacunae separation had a negative correlation with cortical porosity.

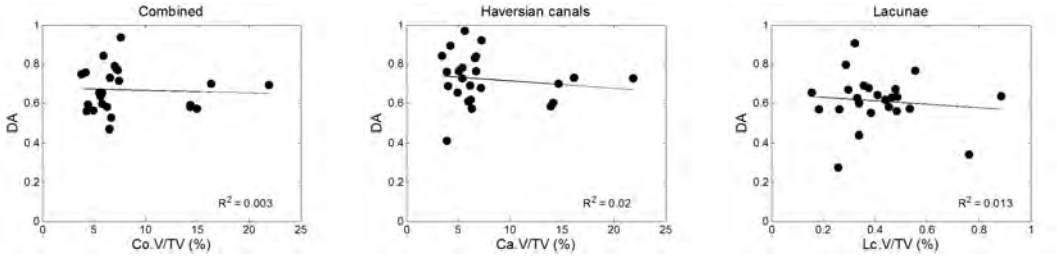

(a) (b) (c)

Figure 32. Degree of anisotropy (DA) vs. cortical porosity for data sets of a) combined, b) Haversian canals and c) lacunae. No correlations were found.

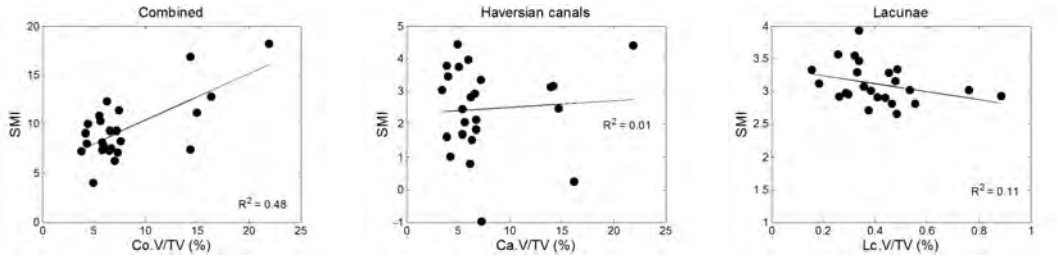

(a) (b) (c)

Figure 33. Structural model index (SMI) for a) combined data set, b) data set including Haversian canals and c) data set including lacunae only. Co.SMI seems to have some linear correlation with the porosity.

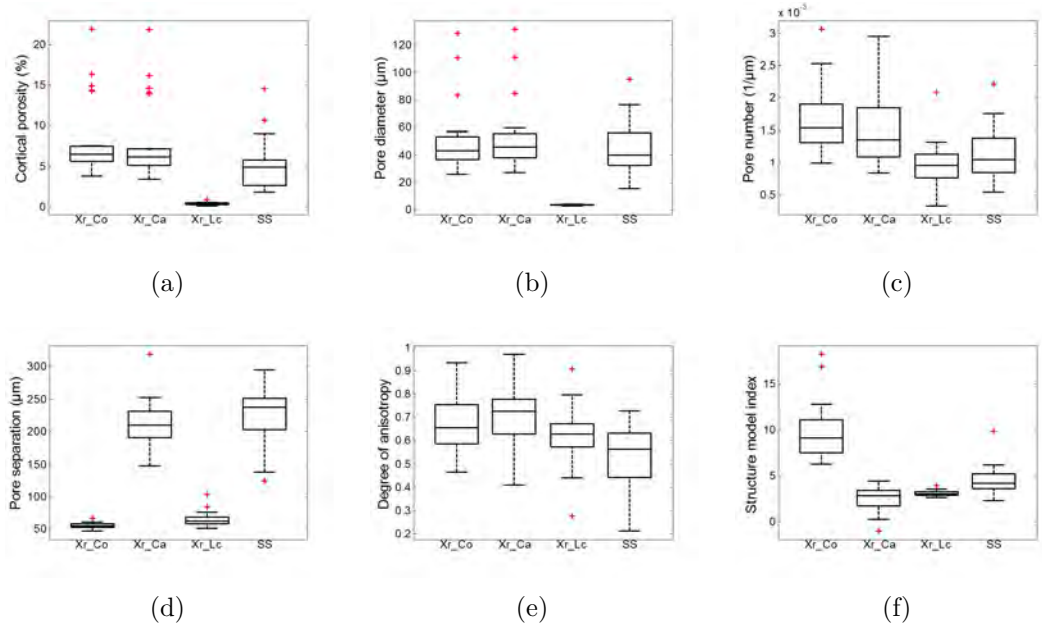

Figure 34. Comparison of the morphological parameters measured with Xradia XCT-400 (Xr) at the University of Jyväskylä (JYU) and with Skyscan (SS) at the University of Eastern Finland (Kuopio). The center line is the median value, the edges of the box are the 25th and 75th percentiles and whiskers are the range of the data set excluding the outliers (red crosses). a) Cortical porosity, b) pore diameter, c) pore number, d) pore separation, e) degree of anisotropy and f) structure model index.

7 Discussion

The first objective of this work was to examine the amount of details we can obtain for human femoral cortical bone samples with the high precision µCT device available at Department of Physics, University of Jyväskylä (JYU). This study was done in collaboration with the University of Eastern Finland (Kuopio) and Lund University (Lund, Sweden), and is related to multi-length-scale analysis of bone fragility properties. A specific objective of high-resolution microtomography imaging was to determine detailed morphological properties of the samples. The most notable parameter determined was the cortical porosity. Porosity was shown to correlate with other properties, such as pore diameter, pore number and structure model index. Statistical analysis was done at three levels of structural hierarchy: one subset of data included only the impact of Haversian canals (abbreviated by Ca), one that of lacunae (Lc) and the third represented a combination of both Ca and Lc (abbreviated by Co with the meaning “combination”). The results for

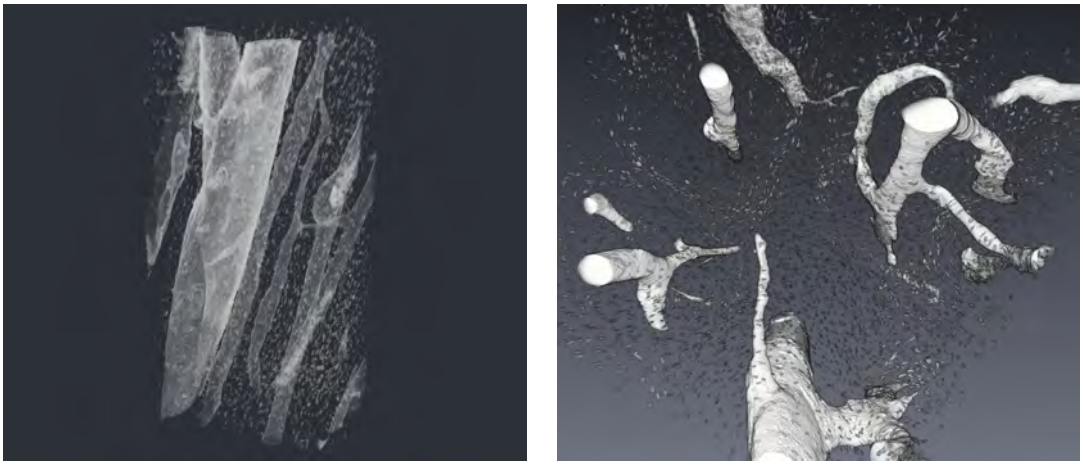

(a) (b)

Figure 35. 3D visualization of the geometry of Haversian canals and lacunae inside the bone: sideview (left) and bottom view (right). The canals slither through the bone along its longitudinal axis. Numerous small dots represent the lacunae. The boundary surface of the bone sample has been excluded for the purpose of visualization.

each data sets were compared with those for SS data. Figure 35 illustrates the formation of intracortical porosity for one sample imaged in this study.

7.1 Evaluation of the methods used and data gathered

In the first part of this work we examined what kind of images we can get by X-ray microtomography using Xradia MicroXCT-400. Cooper *et al.* have indicated that pixel size has a tremendous effect on the values of morphological parameters measured from cortical bone [52]. They measured a set of samples with six voxel sizes, three with different magnifications and three artificially increased from the set scanned with the highest magnification for which the voxel size was 5 µm. The result was that images were more sensitive to changes of magnification rather than to an artificial increase of voxel size. For every voxel size larger than the starting level, the detail patterns were more or less exaggerated, which had an enormous effect on the results. In another article, Kim *et al.* stated that scanning voxel size is the major factor causing the difference of values in cortical porosity and in connectivity density [45]. For canal (or lacunae) diameter and canal (lacunae) surface to volume ratio, both the scanning and reconstruction voxel size had significant effects on the results, whereas the difference in the reconstruction voxel size alone affected the canal (lacunae) number and canal (lacunae) separation. The main

result was that for a bigger voxel size, either in scanning or artificially increased, the difference from the accurate scan increased and led to erroneous results. For lacunae of 10 µm wide, the change of voxel size from 5 to 10 µm decreased the amount of covering pixels from two to one and in the worst case removed small lacunae completely. In the present study, a detector of 40X magnification and a voxel size of 0.31 µm was tested on one sample, but it was noted that these images did not contain significantly more details than those with lower magnification, and had even a smaller field of view (FOV), and thus contained a smaller volume. A detector with 20X magnification and a voxel size of $0.56 - 0.59$ µm was thereby used for every sample. At this scale doubling the voxel size did not affect on the porosity values dramatically since these details of interest were at least one order of magnitude larger, but allowed the FOV to be almost four times larger than that by 40X, allowing thus better statistical analysis.

As a high resolution µCT device, the Xradia MicroXCT-400, had many parameters affecting the image quality. First, the diameter of the sample played a crucial role in the imaging. Preparing samples as handcraft resulted in unidentical diameters, which affected the X-ray absorption and thus the brightness of the image. With proper cutting equipment, the effect of sample size variation could be corrected but at the time of this study there was no suitable tool available. Secondly, the mineral content of different samples may be slightly different which again affects the image brightness and noise level. To provide reference for the bone mineral density in X-ray µCT, a set of mineral density calibration phantoms must be imaged together with each bone sample. In the present case the FOV was limited and there was no space available to include such phantoms. Such phantoms available at the laboratory have a diameter of approximately 2 mm, whereas the FOV was of the order of 1 mm. In this case the main focus was on geometrical imaging rather than quantitative density imaging, to achieve maximal resolution for details such as Haversian canals and lacunae. Thereby the exclusion of density calibration phantoms was not considered crucial. For the same reason, the distances between the sample, radiation source and detector were adjusted separately for each sample. These individualized adjustments were found critical for the image quality.

Individualized tuning of the scanning parameters caused a varying bias in the thresholding of the samples, and thereby a random error in the resulting morphological parameters. This error was shown to be relatively small, only about 4 % (Table 7), corresponding to approximately $0.9 - 12.5$ % of the inter-sample variability in the related data. Tuning of the scanning parameters did not thus significantly affect the results and was thereby justified. Images taken of the samples were clear, and lacunae (diameter approximately 10 µm) were visible and easily distinguishable for further analysis. Image precision was thus satisfactory.

Variability in the scanning parameters led respectively to individualized tuning of the image analysis parameters. One of these latter parameters was the threshold level, on which the impact of variability was tested with visual and analytical methods (Table 8, Figs. 25 and 26). We also tested a fixed threshold level (Fig. 24) which, however, did not permit robust extraction of details from the background noise throughout the samples. The error due to the individualized choice of the threshold level was slightly more than 10 % for the threshold variability of 8 levels while the total volume of the lacunae varied more than 50 %.This is already such a difference that one can distinguish a difference in the quality of images. The actual choice was thus within a narrow range of threshold levels, so as to sufficiently limit the related systematical error in the morphological parameters.

Choosing the proper threshold level was done by visual inspection. Several automated algorithms were tested if they could lead to consistent results. We learned that for this kind of data the automatic approaches cannot correctly separate the details of bone structure from the air and background noise. Some of the algorithms removed almost all of the lacunae and others had trouble with mixing less dense material and air resulting in scattered images. Random errors due to this automated misadjustment were greater than those caused by the human influence of the operator since we defined a narrow range of acceptable threshold levels for the operator, but for the automated tools the range was wide ($99 - 201$). As is evident from Fig. 27, even with the algorithm that gave a threshold closest to that of the visual methods (in this case the method called 'Moments' with a threshold level of 172 while the visually acquired level was 167), the detail resolution and especially the amount of noise in the figure were remarkably different. Operator dependence was not examined in this work.

Note that correlations between morphological parameters and the lacuna volume (and thereby the porosity) were very much as expected. In this case the lacuna diameter (Lc.Dm), number (Lc.N) and structure model index (Lc.SMI) were positively correlated and lacuna separation (Lc.Sp) and degree of anisotropy (Lc.DA) were negatively correlated with the lacuna volume. These correlation results provide guidelines for further statistical analysis based on these data.

Clinical CT devices have been optimized for minimum radiation dose that the patient is exposed to. For high-resolution X-ray CT scanners, such as the Xradia MicroXCT-400 used in this study, the objectives are to maximize the level of details and extensive research utilization as the output power of the X-ray source is not limited by health regulations for living tissue. For the operator the radiation exposure has naturally been minimized by the thick lead enclosure around the radiation source and detector. Shielding combined with correct and careful operation of the device removes efficiently the possible health risk caused by radiation.

The use of micro-CT devices is for *in vitro* studies only. Good resolution requires a narrow radiation beam and small sample size without the distracting soft tissue. A long exposure time leads to an extremely high level of energy per surface area, which also increases the amount of radiation absorbed by the tissue.

7.2 Morphological parameters

Bone fragility increases with age and can be independent of decline in bone mineral density (BMD) [53]. Bone strength is therefore determined by a number of inter-related variables which, in addition to BMD, include bone geometry, bone micro-architecture, bone turnover and the degree of bone mineralization. A specific objective of this work was to determine the micro-architectural attributes of the samples and to determine how these properties correlate with each other.

Cortical porosity is associated to BMD at the macroscopic level and is thus characterized also by the BMD T-score. A healthy cortical wall is solid throughout its thickness and has a sufficiently high level of BMD. While osteoporosis develops, the thickness of the cortical layer decreases. At the same time the diameters of Haversian canals and lacunae increase leading to increased porosity in the periosteal cortical and endosteal trabecular bone. Besides cortical thickness and porosity, BMD is also affected by age and sex of the individual [54].

Macroscale properties such as BMD or, e.g., elastic coefficients can thus be predicted by multiscale models which usually require a large number of parameters to efficiently describe the tissue under examination. The porosity has been proven to be an important determinant of the mesoscopic elastic properties of bone [55]. Properties are mesoscopic when, due to the possible quantum mechanical behavior, macroscale is not precise enough and microscale would be too small to describe the feature in question [56]. However, such properties can be measured with macroscopic techniques since macroscale is heavily dependent on the mesoscopic porperties. The changes in porosity at the microscopic level affects the density and elastic properties at the macroscopic level, which on the other hand defines attributes such as ultrasound velocity and tolerance to mechanical loading. Macroscopic scale and its anisotropic properties can thus be modeled with two parameters of the lower levels: porosity which is known to be an important factor, and mineral content which defines the behavior of the rigid matrix of the bone material [57]. Stiffness coefficients are positively correlated with mineral content and negatively correlated with porosity, and a simple ultrastructure model can be used for the anisotropy at mineralized matrix [58].

The porosity determined in this study had three different levels: The Haversian canals at the 100 µm scale, the lacunae at the 10 µm scale and the combination of

the previous levels. With a spatial resolution of 1.5 µm used in the present study, details smaller than the lacunae, such as canaliculi, were not yet detectable. For each level the same set of mesoscopic morphological parameters were determined, and correlations between the related data across the samples were examined. In this study the porosity was expected to be related to bone mesoscopic elastic parameters such as the Young's modulus, shear modulus and Poisson ratio (Dong *et al.* [55]). These elastic properties were not measured, however. Thus, such comparison between the elastic properties and porosity was not made.

For the twenty-four human cadaveric bone specimens the combined porosity was determined to be $3.79 - 21.93$ % when most of the samples had a porosity between 4 and 8 %. For healthy persons the total cortical porosity is about $4 - 10$ %. Lacuna porosity was $0.12 - 0.84$ % with less variation between samples. For cortical porosity alone, five samples stand out with a higher porosity because an increased volume of canals and two because of an increased volume of lacunae.

Of all the morphological parameters, pore diameter seemed to have the best linear connection with porosity. For Haversian canals this correlation is not a surprise since for the combined volume most of the porosity comes from the canal capacity due to their diameter as the amount of canals was limited to only a few (Tables 13, 14 and Fig. 29). This affected the both two data sets that included Haversian canals. For lacunae the case was different as the porosity was determined by the number of pores since the amount of lacunae was large for volumes of this size, and the diameter did not vary as much as that of the canals (Table 15 and Figs. 29 and 30). Negative correlation between the lacuna porosity and separation (Lc.Sp) was also reasonably explained by porosity: less distance between pores implies more pores inside a volume of interest.

For the samples studied in the present work, the structure model index (SMI) failed to show any difference between the samples. It seems that SMI can have many values independent of porosity (at a fixed scale), and thus any linear correlation of SMI with porosity was not detected. This was the case for all of the three data sets. The most interesting result for the SMI was that its range was lower and narrower for the separated data sets featuring the Haversian canals ($-0.97 - 4.40$) or lacunae ($2.65 - 3.93$) alone, as compared to that for the combined data set ($4.02 - 18.20$). SMI gives some estimation of the structure's resemblance to rods and plates starting from the value 0 for an ideal plate and the value 4 for an ideal sphere in convexity [49]. Negative values represent negative convexity which is an implication of more than 50 % of the relative enclosed cavity volume. Data for the separated data sets of the canals and lacunae can be thought simply as material with either large structures passing through the cavity or small pores dispersed uniformly throughout the bone. When these two subsets are combined

in the combined data set, the structures lose their unambiguousness.

The degree of anisotropy (DA) was shown to be one more attribute which cannot separate the samples in terms of porosity. This is because, during osteoporosis, the number of actual pores does not change the same way as the diameter does. Anisotropy measures equality of the dispersion of pores on a plane perpendicular to the Haversian canals and is linked to homogeneity. Since the orientation of the Haversian canals is the same with the bone's axial orientation, DA shows isotropy for this same direction. DA is an essential determinant of the mechanical properties of bone, such as the strength. The presence of Haversian canals affected the most DA values via their number and diameter. Large and plentiful canals give no intercepts on the test lines in the longitudinal direction, while small serpentine canals give many intercepts. Also lacunae are little more concentrated around the canals, which increases the anisotropy even more. When the canals were subtracted and only the lacunae filled the analyzed volume, bone material seems to be a little more homogeneous and thus isotropic.

There is one particular limitation related to the small size of the VOIs analyzed in this study. The Haversian canals are reasonably large compared to the dimensions of the VOIs, therefore VOIs may not be statistically representative of the individual features of the canal network. To properly represent the natural variations in the density of the canal grid, and in the diameter of the canals, a larger piece of bone may be needed. Although all of the samples were obtained from site-matched locations, the natural variation in the composition of the bone may cause that the canals imaged are not comparable between the donors. The Haversian canals also had a major role as they featured $85.4 - 99.6\,\%$ of the porosity. For a better representation of the canals, the samples should thus be large enough and imaged respectively by a larger voxel size, i.e., lower resolution. This could be done before cutting the samples for imaging at a high resolution.

On the other hand, the present VOIs and resolution were sufficient for imaging of the lacunae. By removing the volume associated to the Haversian canals from the VOIs, we can focus on the local distribution of the lacunae within the resulting sub VOIs. It is expected that the lacunae have a reasonably uniform statistical distribution throughout the cortical bone. Naturally there are local variations between areas next to Haversian canals and areas farther away from them. With the present resolution, it was easy to determine the number and volume of the lacunae. The size of these smaller pores tends to increase during the development of osteoporosis, and thus the lacuna size is expected to include valuable information for characterization of bone fragility. If the aim is to examine both the Haversian canals and the lacunae by a single µCT scan, a compromise between the spatial resolution and VOI must be made. Nevertheless, the voxel size cannot be increased

much of the one used here for the lacunae to be clearly visible.

Comparison between the morphological parameters measured at JYU and Kuopio shows that values acquired from these sets of data have consistent distribution. From the data measured with Xradia XCT-400 (Xr), the Ca set seemed to resemble most resemblance to the Skyscan (SS) data (34). The cortical porosity, pore diameter and pore separation for these two sets were very much alike. For the parameters that were influenced mostly by the Haversian canals, such as pore diameter, the Co set also corresponded well enough with the SS data. It seems that lacunae were not visible in the images taken with Skyscan, since Xr data including lacunae (Co and Lc) had a significantly lower pore diameter than the Ca and SS data. The median values of DA for all of the data were in good accordance, but they covered almost completely the whole range of DA $(0 - 1)$. For separate pore types SMI was close that of the SS data, but the combination set Co gave clearly higher values possibly due to the combination of two different pore sizes.

Despite of consistent distributions, there were no correlations between the data acquired by the two microtomographs. In other words, the results were consistent at the population level but not at the individual level. This can be explained by the limited size of VOI imaged by Xr, which was not large enough to represent the structure of the Haversian canal network. However, we expect Xr scans to provide statistically sufficient volumes to represent the morphology of lacunae, whereas SS was sufficient to describe the Haversian canals. Thereby, it is suggested that the resolution of imaging, and the most suitable device for the purpose, should be chosen based on the length scale of details of interest.

7.3 Concluding remarks and outlook

Generally the data acquisition was, although time consuming, straightforward work which included minor tuning of the parameters due to individual variation between bone samples. Determination of the morphological parameters was also straightforward after the methods for image post processing and binarization had been determined and fixed. It was shown that some of the parameters of the morphological data were correlated with each other according to expectations. The number of samples of this work was sufficient but small for statistical analysis.

In studies related to microtomography it is typical that all of the controllable parameters from imaging to image analysis would be fixed. This was, however, seen to be impossible or impractical with the samples, device and methods of the present study. The samples were extracted from the femora and then cut to the size by coarse methods. Therefore, samples differed a lot from each other with regard to the FOV of the X-ray microtomography scanner. As the main objective

was to obtain high quality projections of three dimensional volumes from the samples, some decisions concerning the scanning parameters, image post processing and analyzer parameters were made. The decisions did result in some amount of operator-dependent uncertainty due to the influence of the operator, but hopefully minimized some artifacts and noise in the images and maximized the detail in the bone composition. In the end it all came down to pore boundary details since the images were binarized by thresholding before the actual analysis.

It seems that in most cases the samples that were particularly porous compared to the average of the data set did not show a linear agreement between the porosity and other morphological parameters. For the pore diameter (for all the data sets: Co, Ca and Lc) the markers of individual samples on the related correlation diagrams followed well the regression line, otherwise the data were clearly separated from the main group and thus from the regression line. This information is suggestive of possible deterioration in the bone condition. Unfortunately, the present number of samples was not sufficient to validate any statistical norms, a large number of samples should be imaged with the same setup to say anything definite. At this stage it would be interesting to compare results of this work with the true condition of the bone to confirm the given speculations.

It was, however, interesting that a sample that had for example distinguishable lacunae porosity also stood out in the total pore separation at the combination level. This supports the objectives of this work by showing that small details have important information and they should not be disregarded.

Most important message of this work is that this kind of study is possible to carry out. The resolution of the scanning device was better than that in most of the previous studies with similar methods and results. The equipment used feature the state of the art and can be used to discover unique features in the structure of different materials. This is a powerful asset which should be used also in the future. It is already possible to go further, since another tomography device working at the $50 - 150$ nanometer scale is available and could be used for the same samples. The uniformity of the lacunae or the mineral composition for example could thus be investigated.

The development of µCT devices has been astonishing during the past few decades. As can be seen from Fig. 36, the detail that can be achieved now is amazing. As high resolution imaging devices are getting common in research laboratories, an increasing number of studies can be made at a fine detail of the bone structure. It is still in debate if the crucial information about diseases such as osteoporosis can be characterized by such a small length scale, or should we look more the big picture, i.e. larger hierarchical length scales. For example, we know that during osteoporosis the porosity of the cortical and trabecular bone changes, and to be

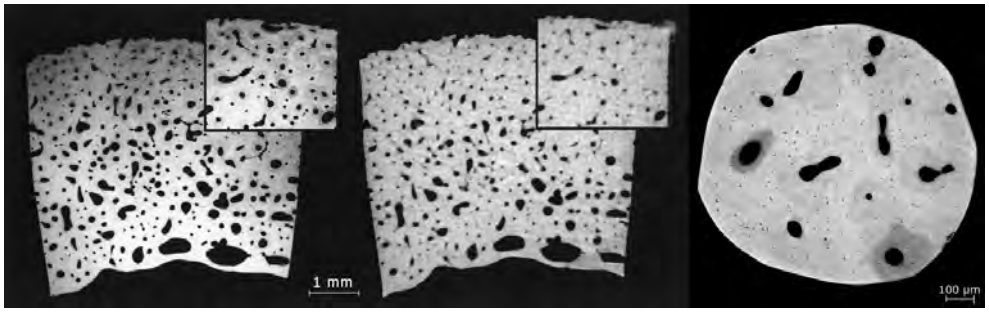

Figure 36. An example of a cross-sectional image sets taken in 2004 with a micro-radiograph (left) and µCT (middle) by Cooper *et al.* [59], and (right) a µCT scan produced in the present study. In both cases the samples were cortical bone. It is evident that a superior detail resolution can be achieved with a good µCT of today in comparison with a radiograph of 2004. Back then the smallest Haversian canals were at the limit of distinguishable detail when today the lacunae have the same status.

able to detect that change the optimal resolution is yet to be determined.

In this study the structure of cortical bone samples was unveiled, and a statistical analysis yielding some morphological parameters was done. The obtained level of fine detail gave new information about the importance of the lacunae and it is clear that there are differences in the microstructure between individuals. Next we should try to understand how the high detailed properties of the bone material correlate with its mechanical properties and phenomena in macroscale. Combining this information with the method of ultrasonic bone assessment being developed by our research group could eventually provide a rapid, inexpensive and precise method for an early detection of the fragility of osteoporotic bone.

References

[1] R. D. Wasnich. Epidemiology of osteoporosis. In M. J. Favus, editor, *Primer on the Metabolic Bone Diseases and Disorders of Mineral Metabolism*. Lippincott, Williams and Wilkins, Philadelphia, fourth edition, 1999.

[2] J. D. Currey. *Bones: structure and mechanics*. Princeton University Press, USA, 2002.

[3] WHO Scientific Group. Prevention and management of osteoporosis. WHO Technical Report Series 921, World Health Organization, Geneva, 2003.

[4] R. Baron. Anatomy and ultrastructure of bone. In M. J. Favus, editor, *Primer on the Metabolic Bone Diseases and Disorders of Mineral Metabolism*. Lippincott, Williams and Wilkins, Philadelphia, fourth edition, 1999.

[5] K. L. Moore and A. F. Dalley. *Clinically oriented anatomy*. Lippincott, Williams and Wilkins, Baltimore, fifth edition, 2006.

[6] F. Kaplan, W. Hayes, T. Keaveny, and *et al.* Form and function of bone. In S. Simon, editor, *Orthopaedic basic science*. American academy of orthopaedic surgeons, Columbus, 1994.

[7] J-Y. Rho, L. Kuhn-Spearing, and P. Zioupos. Mechanical properties and the hierarchial structure of bone. *Medical Engineering & Physics*, 20:92–102, 1998.

[8] P. Moilanen. *Ultrasonic guided wave measurements in bone*. Department of Physics, University of Jyväskylä, 2004. Research Report No. 8/2004.

[9] J. A. Buckwalter, M. J. Glimcher, R. R. Cooper, and R. Recker. Bone biology. part I: structure, blood supply, cells, matrix, and mineralization. *J Bone and Joint Surg*, 77-A:1256–1275, 1995.

[10] J. Karjalainen. *Novel Pulse-Echo Ultrasound Methods for Diagnostics of Osteoporosis*. PhD thesis, 2011.

[11] M. Ramachandran. *Basic Orthopaedic Sciences: The Stanmore Guide*. Hobber Andold Publication, London, 2006.

[12] G. R. Mundy. Bone remodelling. In M. J. Favus, editor, *Primer on the Metabolic Bone Diseases and Disorders of Mineral Metabolism*. Lippincott, Williams and Wilkins, Philadelphia, fourth edition, 1999.

[13] R. B. Martin, D. B. Burr, and N. A. Sharkey. *Skeletal Tissue Mechanics*. Springer-Verlag New York Inc., New York, 1998.

[14] E. Stokstad. Bone quality fills holes in fracture risk. *AAAS Science*, 308:1580–1581, 2005.

[15] B. R. Olsen. Bone morphogenesis and embryologic development. In M. J. Favus, editor, *Primer on the Metabolic Bone Diseases and Disorders of Mineral Metabolism*. Lippincott, Williams and Wilkins, Philadelphia, fourth edition, 1999.

[16] A. M. Parfitt. Age-related structural changes in trabecular and cortical bone: cellular mechanisms and biochemical consequences. *Calcif Tissue Int*, 36(1):S123–S128, 1984.

[17] J. Clifford, M. D. Rosen, and P. Douglas. The aging skeleton. In M. J. Favus, editor, *Primer on the Metabolic Bone Diseases and Disorders of Mineral Metabolism*. Lippincott, Williams and Wilkins, Philadelphia, fourth edition, 1999.

[18] G. P. Liney, C. P. Bernard, D. J. Manton, L. W. Turnbull, and C. M. Langton. Age, gender, and skeletal variation in bone marrow composition: A preliminary study at 3.0 tesla. *J Magn Reson Imaging*, 26(787-93), 2007.

[19] *Diagnosis, prophylaxis, and treatment of osteoporosis*, number 90. Cosensus Development Conference V, 1993, 1994.

[20] R. M. D. Zebaze, A. Ghasem-Zadeh, A. Bohte, and *et al.* Intracortical remodelling and porosity in the distal radius and post-mortem femurs of women: a cross-sectional study. *Lancet*, 375:1729–36, 2010.

[21] C. R. Rosen. Anatomy, physiology and disease. In C. M. Langton and C. F. Njeh, editors, *The Physical Measurement of bone*. Institute of Physics Publishing, Bristol, UK, 2004.

[22] R. Brunader and D. K. Shelton. Radiologic bone assessment in the evaluation of osteoporosis. *Am Fam Physician*, 1;65(7):1357–1365, 2002.

[23] R. Lindsay and F. Cosman. Prevention of osteoporosis. In M. J. Favus, editor, *Primer on the Metabolic Bone Diseases and Disorders of Mineral Metabolism*. Lippincott, Williams and Wilkins, Philadelphia, fourth edition, 1999.

[24] H. H. Bolotin. Dxa in vivo bmd methodology: An erroneous and misleading research and clinical gauge of bone mineral status, bone fragility, and bone remodelling. *Bone*, 41:138–154, 2007.

[25] C. F. Njeh, T. Fuerst, D. Hans, G. M. Blake, and H. K. Genant. Radiation exposure in bone mineral density assessment. *Appl Radiat Isotl*, 50:215–236, 1999.

[26] R. M. Shore and A. K. Poznanski. Radiologic evaluation of bone mineral in children. In M. J. Favus, editor, *Primer on the Metabolic Bone Diseases and Disorders of Mineral Metabolism*. Lippincott, Williams and Wilkins, Philadelphia, fourth edition, 1999.

[27] M-A. Krieg, R. Barkmann, S. Gonnelli, and *et al.* Quantitative ultrasound in the management of osteoporosis: The 2007 ISCD official positions. *Journal of Clinical Densiometry: Assessment of Skeletal Health*, 11(1):163–187, 2008.

[28] P. Moilanen. Ultrasonic guided waves in bone. *IEEE Transactions on Ultrasonics, Ferroelectrics, and Frequency Control*, 55(6):1277–1286, 2008.

[29] G. Boivin and P. J. Meunier. The degree of mineralization of bone tissue mea-

sured by computerized quantitative contact microradiography. *Calcif Tissue Int*, 70:503–511, 2002.

[30] D. Rohrbach, S. Lakshmanan, F. Peyrin, and *et al.* Spatial distribution of tissue level properties in a human femoral cortical bone. *Journal of Biomechanics*, 2012.

[31] K. Raum, I. Leguerney, F. Chandelier, and *et al.* Site-matched assessment of structural and tissue properties of cortical bone using scanning acoustic microscopy and synchrotron radiation μCT. *Phys. Med. Biol.*, 51:733–746, 2006.

[32] H. Oehler, I. Alig, D. Lellinger, and M. Bargmann. Failure modes in organic coatings studied by scanning acoustic microscopy. *Progress in Organic Coatings*, 74:719–725, 2012.

[33] D. Marshall, M. H. Helfrich, and R. M. Aspden. Scanning electron microscopy of bone. In M. H. Helfrich and S. H. Ralston, editors, *Methods in Molecular Medicine, Vol. 80: Bone Research Protocols*. Humana Press Inc., Totowa, NJ, 2003.

[34] P. Sutton-Smith, H. Beard, and N. Fazzalari. Quantitative backscattered electron imaging of bone in proximal femur fragility fracture and medical illness. *Journal of Microscopy*, 229:60–66, 2008.

[35] A. G. Reisinger, D. H. Pahr, and P. K. Zysset. Principal stiffness orientation and degree of anisotropy of human osteons based on nanoindentation in three distinct planes. *Journal of the Mechanical Behavior of Biomedical Materials*, 4:2113–2127, 2011.

[36] O. Pukkila. *Säteily ja ydinturvallisuus, osa 3: Säteilyn käyttö*. Säteilyturvakeskus, Hämeenlinna, 2004.

[37] A. Haavisto, L. Karkela, M. Kervinen, and *et al. maol-taulukot*. Otava, Keuruu, 2001. 1-3. uudistettu painos.

[38] A. G. Webb. *Introduction to Biomedical Imaging*. Number 1. Wiley-iEEE Press, 2003.

[39] R.P.C. Schram. X-ray attenuation, 2011. 20002/01.44395/I.

[40] B. Long. *Complete Digital Photography*. CHARLES RIVER MEDIA, Boston, Massachusetts, fourth edition, 2007.

[41] D. J. Burt. Basic operation of the charge coupled device. In *International Conference on Technology and Applications of Charge Coupled Devices*. University of Edinburgh, Centre for Industrial Consultancy and Liaison, Edinburgh, 1974.

[42] Applied Image Inc., NY, USA. *T-20 USAF 1951 Chart (Standard Layout)*.

[43] F. Natterer and F. Wübbeling. *Mathematical Methods in Image Reconstruction*. SIAM, Philadelphia, 2001.

[44] F. Natterer. *The Mathematics of Computerized Tomography*. SIAM, Philadelphia, 2001.

[45] D-G. Kim, G.T. Christopherson, X. N. Dong, D. P. Fyhrie, and Y.N. Yeni. The effect of microcomputed tomography scanning and reconstruction voxel size on the accuracy of stereological measurements in human cancellous bone. *Bone*, 35:1375 – 1382, 2004.

[46] W. K. Pratt. *Digital image processing : PIKS Scientific inside*. John Wiley & Sons, Inc., Hoboken, New Jersey, fourth edition, 2007.

[47] S. Kaijaluoto. Teknisten ja katsojasta riippuvien tekijöiden vaikutus radiologisten kuvien havainnointiin. Master's thesis, Jyväskylän yliopisto, Fysiikan laitos, 2011.

[48] Xradia, Inc., Concord, CA. *Xradia MicroXCT-200 and MicroXCT-400 User's Guide*, version 7.0, revision 1.5 edition, 2010.

[49] Skyscan. *MORPHOMETRIC PARAMETERS IN CT-ANALYSER: Structural parameters measured by Skyscan™ CT-analyzer software*, 2009.

[50] D. M. L. Cooper, A. L. Turinsky, C. W. Sensen, and B. Hallgrímsson. Quantitative 3D analysis of the canal network in cortical bone by micro-computed tomography. *The Anatomical Record (part B: New Anat.)*, 274B:169–179, 2003.

[51] A. M. Parfitt, M. K. Drezner, F. H. Glorieux, and *et al.* Bone histomorphometry: Standardization of nomenclature, symbols, and units. *Journal of Bone and Mineral Research*, 2(6):595–610, 1987.

[52] D. Cooper, A. Turinsky, C. Sensen, and B. Hallgrimsson. Effect of voxel size on 3D micro-CT analysis of cortical bone porosity. *Calcif. Tissue Int.*, 80:211–219, 2007.

[53] S.L. Hui, C. W. Slemenda, and C. C. Johnston Jr. Age and bone mass as predictors of fracture in a prospective study. *The American Society for Clinical Investigations, Inc.*, 81:1804–1809, 1988.

[54] E. Schoenau, C. M. Neu, F. Rauch, and F. Manz. Gender-specific pubertal changes in volumetric cortical bone mineral density at the proximal radius. *Bone*, 31(1):110–113, 2002.

[55] X. N. Dong and X. E. Guo. The dependence of transversely isotropic elasticity of human femoral cortical bone on porosity. *Journal of Biomechanics*, 37(8):1281–7, 2004.

[56] Q. Grimal, K. Raum, A. Gerisch, and P. Laugier. Derivation of the mesoscopic elasticity tensor of cortical bone from quantitative impedance images at the micron. *Computer Methods in Biomechanics and Biomedical Engineering*, 1, 2008.

[57] M. Granke, Q. Grimal, A. Saïed, P. Nauleau, F. Peyrin, and P. Laugier.

Change in porosity is the major determinant of the variation of cortical bone elasticity at the millimeter scale in aged women. *Bone*, 49(5), 2011.

[58] Q. Grimal, G. Rus, W. Parnell, and P. Laugier. A two-parameter model of the effective elastic tensor for cortical bone. *Journal of Biomechanics*, 44(8), 2011.

[59] D. M. L. Cooper, J. R. Matyas, M. A. Katzenberg, and B. Hallgrimsson. Comparison of microcomputed tomographic and microradiographic measurements of cortical bone porosity. *Calcif Tissue Int*, (74):437–447, 2004.